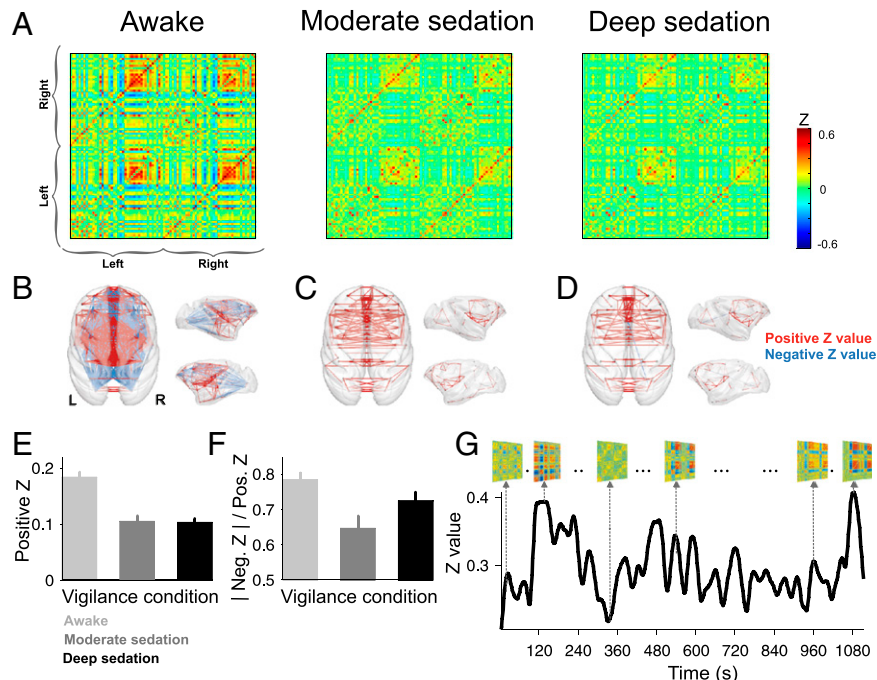


# Correction

## NEUROSCIENCE

Correction for “Signature of consciousness in the dynamics of resting-state brain activity,” by Pablo Barttfeld, Lynn Uhrig, Jacobo D. Sitt, Mariano Sigman, Béchir Jarraya, and Stanislas Dehaene, which appeared in issue 3, January 20, 2015, of *Proc Natl Acad Sci USA* (112:887–892; first published January 5, 2015; 10.1073/pnas.1418031112).

The authors note that Figs. 1 and 2 appeared incorrectly. The corrected figures and their legends appear below.



**Fig. 1.** Stationary functional connectivity as a function of vigilance condition. (A) Average connectivity matrices for all vigilance conditions. (B–D) Brain renders displaying all significant connections ( $P < 0.001$ , FDR corrected) for wake (B), moderate (C), and deep (D) sedation conditions. Red lines represent positive connections between ROIs; blue lines represent negative connections. (E) Average positive z-values within each sedation conditions. In all plots, error bars represent 1 SEM. (F) Ratio of negative to positive z-values. Ratios are calculated for each scanning session, and averaged within each sedation condition. (G) Time course of the L1 norm of the matrix  $Z_{c,s,w}$  for  $w = 1\text{--}464$ , of a sample fMRI session (condition awake, session 14 of monkey J). Inserted matrices show whole brain connectivity patterns at different time points.

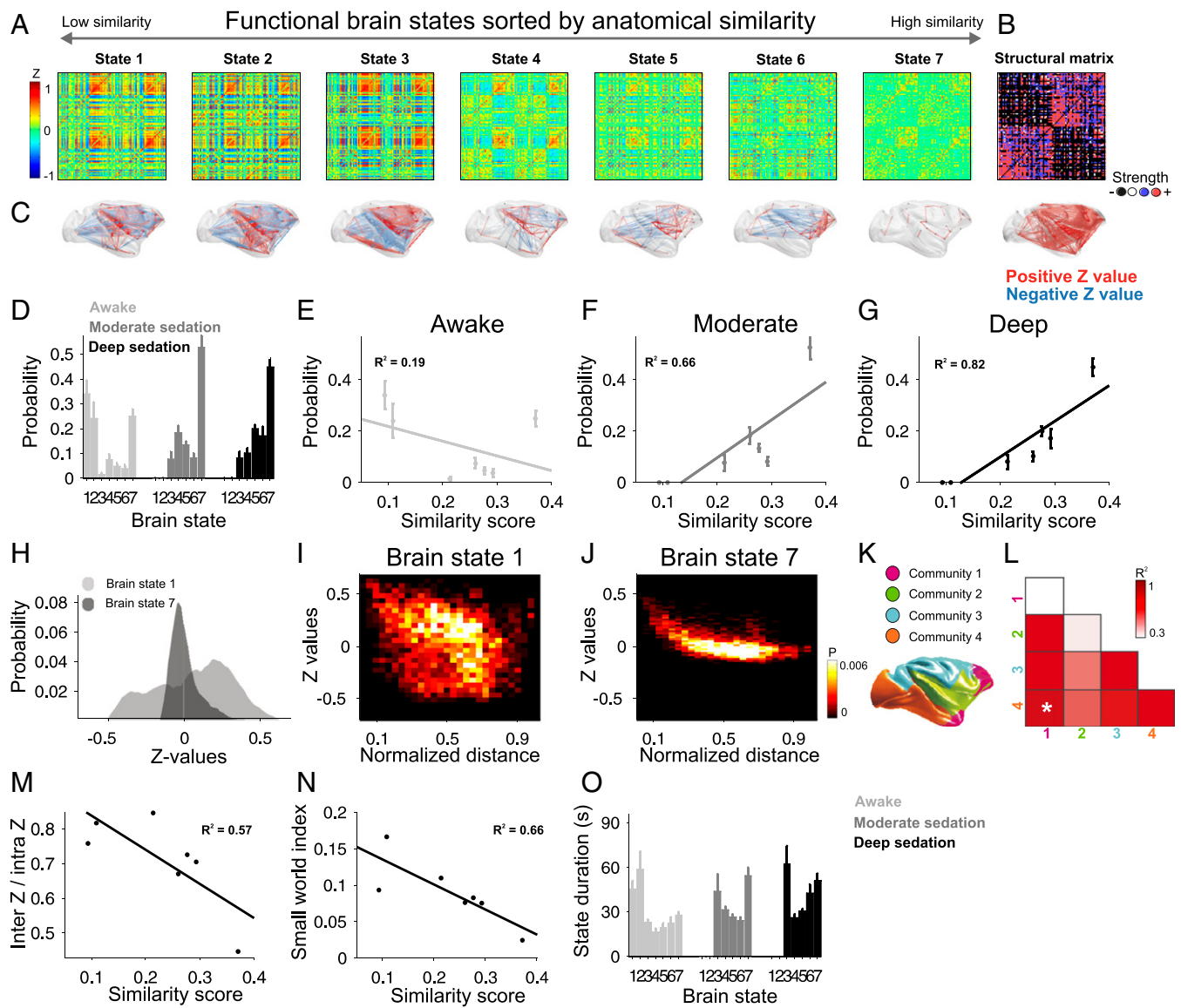


**Fig. 2.** Dynamical connectivity and brain states for all vigilance conditions. (A) Seven brain states, obtained by unsupervised clustering of the  $Z_{cs,w}$  matrix. Brain states are sorted according to their similarity to the structural connectivity matrix. (B) Structural matrix derived from the CoCoMac atlas of anatomical macaque cortical connectivity. Colors represent the four grades of connection intensity (black = 0; white = 1; blue = 2; and red = 3). (C) Brain renders displaying the 400 strongest links, for each brain state. Red lines represent positive connections between ROIs; blue lines represent negative connections. Brain render for the CoCoMac structural matrix displays all links with a value of 3, the maximum value of structural connectivity. (D) Probability distributions of brain states for all vigilance condition. Each bar represents the within-condition probability of occurrence of a state. Error bars stand for SEM. (E–G) Probability of occurrence of each brain state as a function of the similarity between functional and structural connectivity for awake (E), moderate (F), and deep (G) conditions. Each point in the figure corresponds to a brain state, characterized both by a similarity score and a probability of occurrence within each vigilance condition. Error bars show SEM. (H) Probability distribution of all z-values for brain states 1 (the least similar to structure brain state) and 7 (the most similar to structure brain state). (I and J) 2D probability distribution of all z-values for brain state 1 (I) and brain state 7 (J), as a function of the distance of every pair of ROIs. Distance is normalized by the largest distance within the Kotter and Wanke brain atlas. (K) Community decomposition for the Kotter and Wanke brain atlas, taken from Shen et al. (31). Four nonoverlapping communities are defined: frontopolar (community 1), fronto-temporal (community 2), fronto-parietal (community 3), and occipito-temporal (community 4). (L)  $R^2$  value for the regressions between absolute correlation value between ROIs of every pair of communities and similarity score. Asterisks mark significant regression, at  $P < 0.05$  (Bonferroni corrected for multiple comparisons). (M) Ratio between intercommunity z-values and intracommunity z-values for each brain state, as a function of the similarity score. (N) Small world index of all brain states, as a function of the similarity score. Each point represents the small world value of a given brain state. (O) Average life time of brain states for all sedation conditions. Error bars stand for SEM.

[www.pnas.org/cgi/doi/10.1073/pnas.1515029112](http://www.pnas.org/cgi/doi/10.1073/pnas.1515029112)

# Signature of consciousness in the dynamics of resting-state brain activity

Pablo Barttfeld<sup>a,b,1,2</sup>, Lynn Uhrig<sup>a,b,c,1</sup>, Jacobo D. Sitt<sup>a,d,1</sup>, Mariano Sigman<sup>e,f</sup>, Béchir Jarraya<sup>a,c,g,h,2</sup>, and Stanislas Dehaene<sup>a,b,i,j,2</sup>

<sup>a</sup>NeuroSpin Center, Institute of Biologimaging Commissariat à l'Energie Atomique, 91191 Gif/Yvette, France; <sup>b</sup>Cognitive Neuroimaging Unit, INSERM, U992, 91191 Gif/Yvette, France; <sup>c</sup>Avenir-Bettencourt-Schueller Team, INSERM, 91191 Gif-sur-Yvette, France; <sup>d</sup>INSERM, U1127, CNRS UMR 7225, Sorbonne Universités, UPMC Univ Paris 06 UMR S 1127, Institut du Cerveau et de la Moelle Epinière, Institut du Cerveau et de la Moelle Epinière, F-75013 Paris, France;

<sup>e</sup>Laboratorio de Neurociencia Integrativa, Instituto de Física de Buenos Aires, Universidad de Buenos Aires, C1428EGA Buenos Aires, Argentina; <sup>f</sup>Universidad Torcuato Di Tella, C1428BJI Buenos Aires, Argentina; <sup>g</sup>Université Versailles Saint-Quentin-en-Yvelines, 78000 Versailles, France; <sup>h</sup>Neuromodulation Unit, Department of Neurosurgery, Foch Hospital, 92150 Suresnes, France; <sup>i</sup>Université Paris 11, 91405 Orsay, France; and <sup>j</sup>Collège de France, 75005 Paris, France

Edited by Marcus E. Raichle, Washington University in St. Louis, St. Louis, MO, and approved December 4, 2014 (received for review September 19, 2014)

At rest, the brain is traversed by spontaneous functional connectivity patterns. Two hypotheses have been proposed for their origins: they may reflect a continuous stream of ongoing cognitive processes as well as random fluctuations shaped by a fixed anatomical connectivity matrix. Here we show that both sources contribute to the shaping of resting-state networks, yet with distinct contributions during consciousness and anesthesia. We measured dynamical functional connectivity with functional MRI during the resting state in awake and anesthetized monkeys. Under anesthesia, the more frequent functional connectivity patterns inherit the structure of anatomical connectivity, exhibit fewer small-world properties, and lack negative correlations. Conversely, wakefulness is characterized by the sequential exploration of a richer repertoire of functional configurations, often dissimilar to anatomical structure, and comprising positive and negative correlations among brain regions. These results reconcile theories of consciousness with observations of long-range correlation in the anesthetized brain and show that a rich functional dynamics might constitute a signature of consciousness, with potential clinical implications for the detection of awareness in anesthesia and brain-lesioned patients.

脑损伤 由功能网络的变化(对比)  
consciousness | functional connectivity | structural connectivity | 正常来判断病人脑损伤程度  
dynamics | anesthesia

During the awake resting state, spontaneous brain activity is highly structured. Functional MRI (fMRI) recordings indicate that brain activity constantly waxes and wanes in a tightly correlated manner across distant brain regions, forming reproducible patterns of functional connectivity that exhibit both a rich temporal dynamics (1, 2) and spatial organization into functional networks (3, 4). Ever since the discovery of these resting state patterns, their interpretation has been debated. Many of these patterns match those observed during active cognitive tasks, suggesting that they might arise from a spontaneous, endogenous activation of cognitive processes (5, 6). Indeed, the default mode network (DMN), the most prominent functional network at rest, is most active when subjects direct attention to inward processes, such as daydreaming or imagining (6). Furthermore, when a subject is interrupted during the resting state, functional connectivity patterns at the time of interruption can partially predict whether a subject was imagining or mind wandering (7, 8), and what was the focus of attention (9).

Although these findings show that part of the resting state brain activity, at least, indexes ongoing mental content, this conclusion appears to be in conflict with other studies showing that long-range resting-state functional connectivity persists even after loss of consciousness (LOC) due to general anesthesia (10, 11) or in vegetative state (VS) patients (12, 13). Although a small proportion of VS patients show a high degree of residual cognitive activity (14, 15), this is unlikely to be the case during general anesthesia, suggesting that complex functional connectivity patterns can also arise purely as the result of a semirandom

circulation of spontaneous neural activity along fixed anatomical routes. Indeed, mean-field simulations models of resting state brain activity provide a relatively good match to the observed static functional connectivity patterns by simply implementing a noisy reverberation within the known whole-brain connectivity matrix, without making any specific assumption about ongoing cognitive processes (16, 17).

These studies raise the following questions. Is resting-state activity a mere manifestation of the organized structural connectivity matrix, which is hence preserved even in absence of consciousness, for instance, during general anesthesia? Or alternatively, do some aspects of resting state brain activity specifically reflect the flow of cognitive processes that characterizes the conscious state? If so, how should functional connectivity data be processed to extract signatures of the conscious state, i.e., features of resting state activity that are only present in the awake state and disappear with the loss of consciousness? Identifying such signatures may have important consequences for clinical practice, as it would add to the small number of brain-imaging paradigms that are currently available to diagnose residual consciousness in VS patients (15, 18–20).

Here, we set out to address these questions by comparing fMRI images of spontaneous fluctuations in monkey brain activity either in the awake state or while undergoing general anesthesia. Our working hypothesis, based on dynamical systems

## Significance

What are the origins of resting-state functional connectivity patterns? One dominating view is that they index ongoing cognitive processes. However, this conclusion is in conflict with studies showing that long-range functional connectivity persists after loss of consciousness, possibly reflecting structural connectivity maps. In this work we respond to this question showing that in fact both sources have a clear and separable contribution to resting-state patterns. We show that under anesthesia, the dominating functional configurations have low information capacity and lack negative correlations. Importantly, they are rigid, tied to the anatomical map. Conversely, wakefulness is characterized by the dynamical exploration of a rich, flexible repertoire of functional configurations. These dynamical properties constitute a signature of consciousness.

Author contributions: B.J. and S.D. designed research; L.U. performed research; P.B., J.D.S., M.S., and S.D. analyzed data; and P.B., L.U., J.D.S., M.S., B.J., and S.D. wrote the paper.

The authors declare no conflict of interest.

This article is a PNAS Direct Submission.

<sup>1</sup>P.B., L.U., and J.D.S. contributed equally to this work.

<sup>2</sup>To whom correspondence may be addressed. Email: pablo.barttfeld@cea.fr, bechir.jarraya@cea.fr, or stanislas.dehaene@cea.fr.

This article contains supporting information online at [www.pnas.org/lookup/suppl/doi:10.1073/pnas.1418031112/-DCSupplemental](http://www.pnas.org/lookup/suppl/doi:10.1073/pnas.1418031112/-DCSupplemental).

simulations of resting state brain activity (16, 21–24), is that signatures of the conscious state lie in the dynamics of spontaneous brain activity. When averaged across a long time period, functional brain activity may appear similar in wakefulness and anesthesia (10, 11, 25), due to the existence of a backbone anatomical connectivity. However, the implicit assumption of temporal stationarity underlying typical resting state analyses, while useful, might provide a wrong image of the underlying functional configurations (just like the averaged outcome of tossing a fair coin, i.e., 50% heads, may not even be a possible state of the world). Indeed, several techniques have recently emerged to avoid the temporal averaging step and replace it with a direct visualization of the temporal dynamics of spontaneous brain activity patterns (26–28). These techniques have revealed a far richer picture of the nature, duration, and transition probabilities of human resting state activity in the awake condition (26–28), but they have not yet been applied to the identification of how these characteristics change during the loss of consciousness.

Theories and simulations of brain operations suggest that the temporal dynamics of brain networks should be very different during wakefulness and after loss of consciousness due to anesthesia, coma, or sleep. The awake condition should be characterized by an active exploration of a high diversity of network states (22–24), forming the ceaselessly fluctuating “stream of consciousness” described by William James. During the non-conscious condition, however, spontaneous activity should reduce to the circulation of a more random pattern of neural activity shaped and constrained by the anatomical connectivity (17, 21). According to this view, the role of structural connectivity in sculpting functional connectivity maps should vary during wakefulness and anesthesia. Although wakefulness should be characterized by a rich repertoire of connectivity patterns (23), the functional connectivity patterns of the sedated brain should highly resemble the underlying structural map (16).

## Results

We compared the dynamics of resting state fMRI networks in macaque monkeys (*Macaca mulatta*) under three levels of vigilance: the awake resting state and two levels of propofol sedation (moderate and deep; *SI Materials and Methods* and *Table S1*). Functional connectivity was measured between 82 previously defined cortical regions of interest (ROIs) (*Table S2*) for which an approximate matrix of intra- and interhemispheric anatomical connectivity is available, based on a large number of previous tracer studies (*CoCoMac* database) (29).

For reference, we first measured the classical time-averaged stationary pattern of functional correlations. To this aim, we estimated the Fisher-transformed covariance matrix  $Z_{c,s}$  for each vigilance condition  $c$  and session  $s$ . The matrix entry  $Z_{c,s}(i,j)$  indicates the temporal covariance of the average fMRI signal of ROIs  $i$  and  $j$  throughout an entire fMRI session (20 min) (Fig. 1A). This static analysis confirmed the persistence of long-range stationary connections under anesthesia (10, 11), involving key nodes of the default-mode network (Fig. 1B–D). In the awake condition, we observed a positive cluster of connections localized mainly to frontal and midline cortical regions. Positive connections formed a complex long-distance graph including anterior and posterior cingulate cortex, dorsomedial prefrontal cortex, as well as nodes in peripheral areas such as primary motor, sensorimotor, and auditory cortices (see *Table S3* for a list of the most connected ROIs). In the awake resting state, a large number of negative connections spread more broadly projecting to the more posterior regions of the brain. In the two levels of sedation we still observed a large number of significant correlations, but the vast majority were positive (Fig. 1C and D).

Quantification and statistical analysis of those results indicated that the stationary connectivity matrix provided only partial indications of the state of consciousness. The average positive

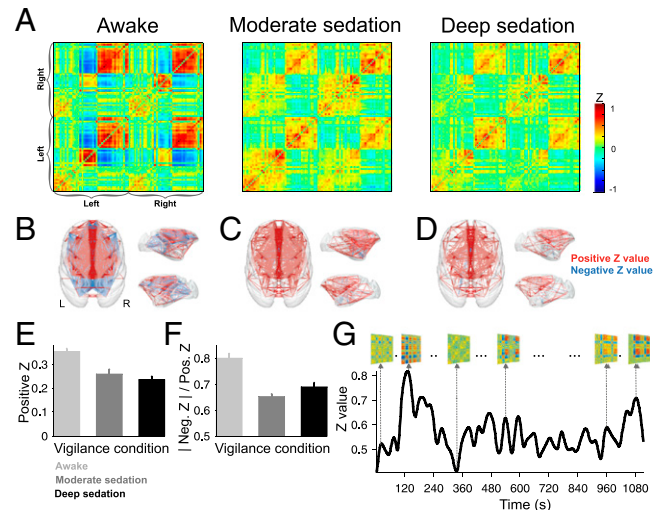


**Fig. 1.** Stationary functional connectivity as a function of vigilance condition. (A) Average connectivity matrices for all vigilance conditions. (B–D) Brain renders displaying all significant connections ( $P < 0.001$ , FDR corrected) for wake (B), moderate (C), and deep (D) sedation conditions. Red lines represent positive connections between ROIs; blue lines represent negative connections. (E) Average positive z-values within each sedation conditions. In all plots, error bars represent 1 SEM. (F) Ratio of negative to positive z-values. Ratios are calculated for each scanning session, and averaged within each sedation condition. (G) Time course of the L1 norm of the matrix  $Z_{c,s,w}$  for  $w = 1\text{--}464$ , of a sample fMRI session (condition awake, session 14 of monkey J). Inserted matrices show whole brain connectivity patterns at different time points.

z-value diminished under sedation compared with the awake condition (Fig. 1E; awake vs. moderate sedation, bootstrap analysis,  $P < 10^{-3}$ ; *SI Materials and Methods*; awake vs. deep sedation,  $P < 10^{-4}$ ), but there were no significant differences between both sedation conditions (moderate sedation vs. deep sedation,  $P > 0.1$ ). The ratio of negative to positive correlations also diminished significantly in sedation conditions compared with the awake condition (Fig. 1F; awake vs. moderate sedation,  $P < 10^{-3}$ ; awake vs. deep sedation,  $P < 10^{-4}$ ) and, marginally, between sedation conditions (moderate sedation vs. deep sedation,  $P < 0.05$ ). Thus, under anesthesia, brain regions tended to be more weakly coupled than in the wake condition, and most of the negative correlations were lost.

Next we tested the prediction that the temporal dynamics of brain connectivity would sharply vary with the level of vigilance. For this, following the procedure described by Allen et al. (26), we estimated sliding window Fisher-transformed covariance matrices  $Z_{c,s,w}$ , for each fMRI vigilance condition  $c$ , session  $s$ , and time window  $w$  (26, 30) (similar results were obtained using the inverse covariance matrix; *SI Materials and Methods*). As recently reported (26–28), the covariance between specific ROI pairs, as well as the whole-brain average of the covariance, constantly varied over time (Fig. 1G and *Movie S1*). We identified the dominant recurrent patterns of brain connectivity [referred to as brain states (BSs)] by means of an unsupervised clustering method along the time dimension of the  $Z_{c,s,w}$  matrix (26). To avoid any bias, this analysis was performed on the data from all vigilance conditions mixed. As in previous studies (26), we set the predefined number of brain states  $n$  to 7, but varying the number of states did not change any of the main findings reported here (*Fig. S1*). The method provides, for each point in time, the most likely state of functional connectivity, allowing us to compare how these states and their dynamics vary with the level of vigilance.

To evaluate whether dynamic long-range connectivity reduces to the underlying structural connectivity map specifically during loss of consciousness, we ranked all brain states (Fig. 2A and Fig. S2) according to their similarity (Fig. S3 and *SI Materials and Methods*) to the CoCoMac (29) structural connectivity matrix (Fig. 2B and Fig. S4). We then explored how the probability of occurrence of each brain state varied with the vigilance condition. Probability of occurrence of brain state  $n$  was estimated as the proportion of times each matrix  $Z_{c,s,w}$  was classified as belonging to that brain state. In the awake condition, most brain states (except brain states 3 and 4) had a similar probability of occurrence, and this probability was not modulated by the similarity of the functional network to structural connectivity ( $\beta$ -value = 0.049;  $R^2$  = 0.001;  $P > 0.9$ ; Fig. 2D and E). In contrast, the probability distribution of brain states was heavily reshaped under sedation (Fig. 2D, F, and G): the more similar a brain state of functional connectivity was to structural connectivity, the more probable it became under sedation (regression analysis; moderate sedation:  $\beta$ -value = 0.66;  $R^2$  = 0.93;  $P < 10^{-3}$ ; deep sedation:  $\beta$ -value = 0.53;  $R^2$  = 0.87;  $P < 10^{-2}$ ; Fig. 2F and G). To quantify this, we ran a fixed effect ANOVA on mean rank similarity as function of vigilance level (where rank 7 is the

closest to the anatomical connectivity matrix). The change in brain state composition was significantly altered by sedation [mean rank: awake = 4.25; moderate sedation = 5.20; deep sedation = 5.73;  $F_{(2,74)} = 30.51$ ,  $P < 10^{-8}$ ]. In fact, the occurrence probability of some brain states, notably states 1 and 2 with the lowest similarity, was so low that they never occurred during sedation. Correspondingly, brain state 7, most similar to anatomical structure, became functionally dominant and its occurrence probability was strongly modulated by vigilance level [ANOVA mean rank similarity; mean rank: awake = 0.16; moderate sedation = 0.41; deep sedation = 0.48;  $F_{(2,74)} = 19.08$ ,  $P < 10^{-6}$ ; Fig. 2F and G].

Having identified brain states that are either typical of conscious function or dominant during sedation, we next sought to understand how their network properties and topology differed. First, we calculated for each brain state  $n$  the average absolute covariance  $c_{ij}$  linking each ROI  $j$  to all other ROIs (*SI Materials and Methods*), an estimate of the average functional coupling for this brain region. Across the seven brain states, the  $c_{ij}$  value decreased with increasing similarity to anatomy (regression analysis;  $\beta$ -value = -0.81;  $R^2$  = 0.84,  $P < 0.005$ ). This observation showed that the larger the similarity score, and therefore the more probable a brain state under anesthesia, the weaker the

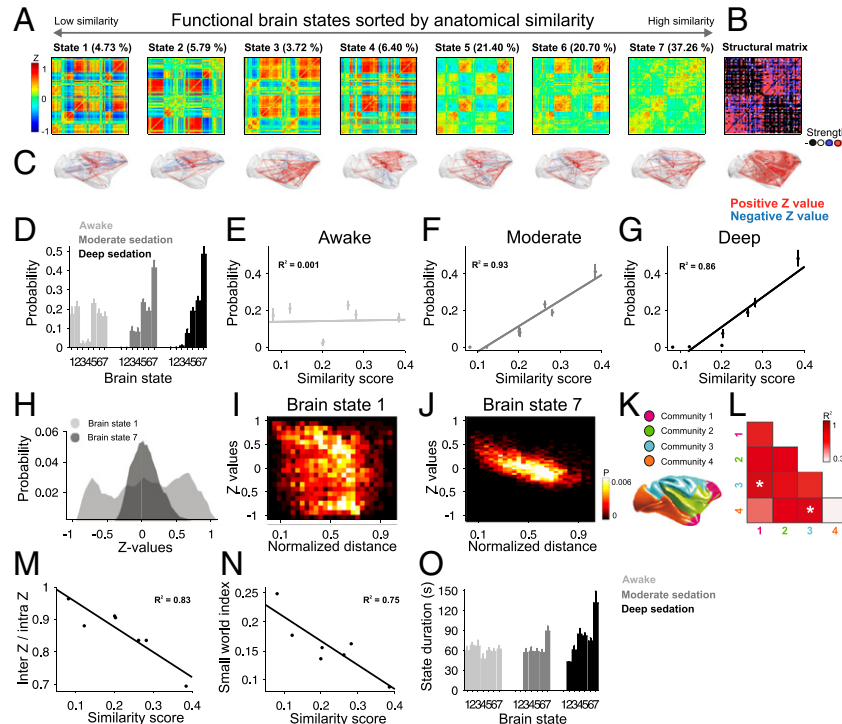


**Fig. 2.** Dynamical connectivity and brain states for all vigilance conditions. (A) Seven brain states, obtained by unsupervised clustering of the  $Z_{c,s,w}$  matrix. Brain states are sorted according to their similarity to the structural connectivity matrix. Colors represent the four grades of connection intensity (black = 0; white = 1; blue = 2; and red = 3). (C) Brain renders displaying the 400 strongest links, for each brain state. Red lines represent positive connections between ROIs; blue lines represent negative connections. Brain render for the CoCoMac structural matrix displays all links with a value of 3, the maximum value of structural connectivity. (D) Probability distributions of brain states for all vigilance condition. Each bar represents the within-condition probability of occurrence of a state. Error bars stand for SEM. (E–G) Probability of occurrence of each brain state as a function of the similarity between functional and structural connectivity for awake (E), moderate (F), and deep (G) conditions. Each point in the figure corresponds to a brain state, characterized both by a similarity score and a probability of occurrence within each vigilance condition. Error bars show SEM. (H) Probability distribution of all z-values for brain states 1 (the least similar to structure brain state) and 7 (the most similar to structure brain state). (I and J) 2D probability distribution of all z-values for brain state 1 (I) and brain state 7 (J), as a function of the distance of every pair of ROIs. Distance is normalized by the largest distance within the Kotter and Wanke brain atlas. (K) Community decomposition for the Kotter and Wanke brain atlas, taken from Shen et al. (31). Four nonoverlapping communities are defined: frontopolar (community 1), fronto-temporal (community 2), fronto-parietal (community 3), and occipito-temporal (community 4). (L)  $R^2$  value for the regressions between absolute correlation value between ROIs of every pair of communities and similarity score. Asterisks mark significant regression, at  $P < 0.05$  (Bonferroni corrected for multiple comparisons). (M) Ratio between intercommunity z-values and intracommunity z-values for each brain state, as a function of the similarity score. (N) Small world index of all brain states, as a function of the similarity score. Each point represents the small world value of a given brain state. (O) Average life time of brain states for all sedation conditions. Error bars stand for SEM.

functional coupling between brain regions. Indeed, the SD of the distribution of functional connectivity values increased as the similarity score decreased ( $\beta$ -value =  $-1.54$ ;  $R^2 = 0.86$ ,  $P < 0.01$ ), reflecting a decrease in the number of connections with strongly positive ( $\beta$ -value =  $-0.76$ ;  $R^2 = 0.78$ ,  $P < 0.01$ ) and, most notably, strongly negative ( $\beta$ -value =  $-0.83$ ;  $R^2 = 0.92$ ,  $P < 10^{-3}$ ) weights. The change in SD of distribution is clearly visible when comparing the histogram of functional connectivity measures for brain states 7 (most frequent under sedation) and 1 (least frequent) (Fig. 2H). Although the distribution of z-values of brain state 7 was single-peaked and close to a Gaussian distribution centered on zero, indicating low and sparse connectivity, the distribution for brain state 1 was two-peaked, evidencing the presence of strong functional correlations and anticorrelations unique to the awake condition.

We further analyzed how functional connectivity varied with the spatial distance between two brain regions in all brain states. For brain state 1, connectivity strength decreased only moderately with distance, and dense strong connections (positive and negative) were observed even for very distal pairs of nodes (Fig. 2J). Brain state 7 showed a very different pattern (Fig. 2J), with a predominance of short-range strong connections and a functional connectivity dropping to zero as distance increases. Statistical analysis revealed a monotonic decrement in connectivity strength as a function of distance along the similarity axis: whereas z-values decreased with distance for all brain states, the more similar a brain state was to structure, the faster correlations decayed with distance ( $\beta$ -value =  $-0.48$ ;  $R^2 = 0.77$ ,  $P < 0.01$ ).

We next investigated the topological properties of brain states. To this aim, we used a preexisting partition of the ROI set into communities (31) (Fig. 2K). Community decomposition subdivides the matrix into nonoverlapping groups of ROIs in a way that maximizes the number of within-group edges and minimizes the number of between-group edges (3, 32) (see Table S2 for the community membership of each ROI). In accordance with our previous results, we observed that the absolute value of correlation between any pair of communities diminished along the similarity axis, but this diminution was only significant after Bonferroni correction for the pairs linking community 3 (fronto-parietal) with communities 1 (frontopolar) and 4 (occipito-temporal) (Fig. 2L;  $P < 0.05$ , Bonferroni corrected). Furthermore, the ratio between intermodule and intramodule correlation monotonically diminished as similarity score increased (Fig. 2M;  $\beta$ -value =  $-1.07$ ;  $R^2 = 0.83$ ,  $P < 0.01$ ). Importantly, inter-module correlations were negative on average for all brain states, i.e., the ratio of negative intermodule and negative intramodule correlations was higher than 1 for all brain states. Thus, under sedation, the brain functional networks disaggregate into a preexisting set of functional backbone modules.

The observed changes in functional topology suggest that sedation leads to a drop in the overall level of integration of brain areas into an efficient network. We quantified this through the Small World (SM) index, which quantifies the optimality of a network in terms of integration (measuring distance between nodes) and segregation (measuring the tendency of a network to form clusters of nodes) (3, 33). We found that, even after normalizing brain states by the strength of connections to rule out trivial differences, the SM index diminished monotonically as the similarity score increased (Fig. 2N;  $\beta$ -value =  $-1.82$ ;  $R^2 = 0.75$ ;  $P < 0.02$ ): the more similar to structure a brain state is and therefore the more likely it is to dominate in the sedated brain, the lower its network capacity. Recent anatomical observations concur with the present results in suggesting that the structural network of the macaque brain does not fit well with a SM architecture (34). Crucially, our results show that, in the wake condition only, the constantly fluctuating functional networks that ride on top of this fixed architecture constitute a better approximation of this optimal communication structure (3, 33).

We next analyzed the average time duration of each brain state (or, equivalently, the probability that a state  $BS_n$  is followed by itself) as a way to estimate the stability of dynamical connectivity. Sedation increased the average duration of brain states, even after subtracting the duration increment explained by the increased presence of certain states (Fig. 2O; bootstrap analysis; awake vs. moderate sedation,  $P < 0.05$ ; awake vs. deep sedation,  $P < 10^{-4}$ ; moderate sedation vs. deep sedation,  $P < 10^{-4}$ ). These changes are mostly explained by the increased duration of brain state 7 that dominates during deep sedation (Fig. 2O).

To further characterize the temporal dynamics of brain states, we conducted a detrended fluctuation analysis (DFA; *SI Materials and Methods*) to estimate the degree of autocorrelation in the time series giving rise to different brain states. For each session and each time series, we used DFA to estimate the Hurst exponent ( $H$ ).  $H$  measures the amount and type of autocorrelation present in a time series. An  $H$  value larger than 0.5 indicates that the time series is correlated in time, whereas an  $H$  value of 0.5 indicates that the time series is close to white noise, exhibiting no correlation in time.  $H$  was significantly lower during deep sedation than in the awake condition (Fig. S5 A and B) ( $H_{awake} = 0.772$ ;  $H_{deep} = 0.722$ ; bootstrap analysis,  $P = 0.03$ ), and marginally lower in moderate sedation than in awake ( $H_{moderate} = 0.724$ ; bootstrap analysis,  $P = 0.05$ ) but did not differ significantly between sedation conditions ( $P > 0.1$ ). The drop in  $H$  value indicates, in agreement with previous work on sleep (35) and anesthesia (36), that there is a breakdown of temporal integration in the sedated brain. To relate the fluctuations in  $H$  value over different sessions with fluctuations in brain states, we calculated for every session the mean similarity score index, or the average similarity to the anatomical connectivity matrix score across all brain states present in a single session. A session composed almost entirely of brain state 7 will thus have a higher similarity score than a session composed mainly of brain states 1 and 2, which are most different from structural connectivity. We found that the higher the mean similarity score in a given session, the lower the  $H$  value (Fig. S5 C and D; regression analysis across all sessions:  $\beta$ -value =  $-0.20$ ;  $R^2 = 0.18$ ;  $P = 10^{-4}$ ). This observation shows that the brain states closest to structure, those that dominate under sedation, arise from time series that increasingly lack a temporal memory (as their Hurst exponent  $H$  moves closer to 0.5) and thus increasingly resemble a semirandom circulation of spontaneous neural activity.

## Discussion

As previously suggested by experiments in sedated rats and monkeys (10, 11), our results reveal that under general anesthesia, spontaneous brain activity converges to a few or even a single dominant brain dynamical pattern, still characterized by a broad set of long-range functional connections, but with weak, positive, nonspecific couplings that rigidly parallel the underlying structural map. Above and beyond this conclusion, here we demonstrate that the sedated state is characterized by a radical change in brain dynamics, with a drastic reduction in the spontaneous temporal exploration of many different brain configurations. By acquiring, in the same monkeys, fMRI images of awake and sedated spontaneous activity in the entire brain and decomposing these signals over time, we observed a much greater diversity of brain states during wakefulness.

Our results do not merely reflect a slowing down of brain activity. First, in each fMRI run, we compute the functional connectivity states over a full 20 min of fMRI data. If the anesthetized brain presented the same set of states and merely took a longer time to move from one state to the other, the same overall set of states would be eventually detected. What we see instead is a radical change in the distribution of states and the dominance of a very small set of states closely resembling the anatomical connectivity matrix. To further rule out the possibility that our results arise from slower interactions between brain areas

under sedation, we conducted a lagged-correlation analysis that allowed for lags of up to two samples (4.8 s) between brain regions. The results were extremely similar to the zero-lag analysis (Fig. S6 and *SI Materials and Methods*), showing that the changes related to sedation are not simply due to a slower dynamics.

Our findings fit squarely with dynamical systems simulations of resting state brain activity (16, 21, 37). Such simulations have established that, for low coupling strength between brain areas—a configuration that resembles the sedated condition—spontaneous neuronal activity is still present but mostly traces the fixed network defined by structural connectivity, and as a result, only a single stable spontaneous connectivity pattern occurs (16, 17). As the coupling strength increases, a qualitative change in the dynamics occurs: instead of having a single stable state, the system becomes multistable; functional activity spontaneously breaks down into a diversity of states that is sequentially explored in a stochastic manner (16, 21, 23, 37, 38). It has been argued that the brain operates precisely at the edge of this dynamical change—or critical state (39)—in which the system is maximally sensitive to external stimulation.

An interesting apparent paradox arises from our results: although the brain states closer to structure become more prominent and more durable under sedation, the Hurst exponent associated with the sedation conditions, and specifically with those brain states closest to structure, is relatively low compared with the awake condition, indicating a reduced temporal autocorrelation. The latter observation is consistent with the literature on sleep (35) and anesthesia (36): a loss of consciousness is associated with a drop in  $H$  value toward 0.5, the value that arises when the dynamics of time series is close to white noise, lacking temporal memory. How could more stable brain states arise from noisier and increasingly memoryless time series? A possible explanation comes again from dynamical systems modeling (16). As mentioned, for low coupling strength between brain areas, a single stable spontaneous connectivity pattern exists. Because it becomes the only available attractor, the sedated brain cannot depart from it and remains confined to a semirandom exploration of the valley surrounding it, thus simultaneously exhibiting interregional correlations along fixed anatomical routes and a memoryless trajectory with diminished autocorrelation.

Our results are also in agreement with several theories of consciousness (22, 24) and earlier observations in sleep, anesthesia, and VS (18, 40–43). Several theories of consciousness posit that distributed functional networks support conscious states and that loss of consciousness is indexed by alterations of these network patterns (22, 24, 42). According to these theories, the functional networks that support consciousness must display both global integration—evidenced as a strong coupling between long-distance brain regions—and a large repertoire of heterogeneous functional states of activity (44). In full agreement with these ideas, our results show that the brain functional configurations that characterize the sedated condition exhibit persisting long-range connections along structural pathways but lack both strong coupling and a rich repertoire of cognitive states.

Importantly, because the data were processed identically in all conditions, the changes we observe across conditions cannot be attributed to commonly discussed methodological artifacts. In particular, we observed that the presence of negative correlations is characteristic of wakefulness. Anticorrelations between task-negative and task-positive networks have long been reported to occur during both wakeful rest and the performance of specific cognitive tasks (2), but their importance in the functional connectivity matrix has been debated in the past, because such negative links could be partially induced by temporal filtering and other data processing techniques such as subtraction of the overall mean brain activity (45). Here we show that, for a constant data processing strategy, negative functional correlations between regions are virtually absent in the anesthetized brain

and become significantly increased in the awake brain. This observation implies that such negative or anticorrelations cannot be entirely imputed to artifacts of the analysis method, but are a genuine characteristic of the conscious resting brain that vanishes during anesthesia. It appears that during conscious rest, among the many potential brain activity states that are afforded by the static connectivity matrix, a subset of active areas is selected at a given moment, whereas others are actively extinguished, giving rise to a characteristic pattern of positive and negative links. This finding also fits with the Global Neuronal Workspace theory (22), according to which the “ignition” of a global neural state coding for a particularly conscious content leads to the active inhibition of other potential contents (37) and therefore induces a central bottleneck in dual-task processing (46, 47).

An important consequence of the present results, which should be tested in future research, is that the temporal dynamics of spontaneous brain activity, measured using the entropy of the state transition matrix, might supplement existing tools (18, 19, 42) as a clinically useful index of consciousness in vegetative patients and during anesthesia. Detecting residual consciousness in patients remains a difficult clinical problem, as it has been determined that as many as 40% of locked-in syndrome patients (who are fully conscious) initially fail to be detected, even in experienced clinical centers (48), and some patients in an apparent VS may simply lack any of the behavioral means of manifesting their preserved consciousness to their surroundings (14, 15). Several brain-imaging tests are now available to detect residual signs of consciousness, but the vast majority of them require subjects to perform a demanding cognitive task [e.g., imagining playing tennis (15), counting rare sounds (49), or watching a Hitchcock movie (20)]. Only recently have purely passive tests been proposed, based solely on the quantification of the propagation of activity in distributed areas of the cortex (18, 42). The present work opens up the possibility that residual consciousness could be quantified by simply monitoring the dynamics of resting state activity. More specifically, it suggests that the mere presence of long-distance functional connectivity networks may not be a sufficient condition (50–52), as it may simply arise as a result of a shaping of nonconscious spontaneous activity by the preserved anatomical connectivity matrix. Rather, our results point to the importance of developing analytic tools to capture the dynamics of brain activity (26–28) and tentatively suggests that entropy of the state transition matrix, distance of each state to the underlying anatomical connectivity matrix, and presence of negative links may serve as useful candidate signatures of consciousness.

## Materials and Methods

**Animals.** Three rhesus macaques (*Macaca mulatta*; one male and two females, monkeys J, K, and R; 5–8 kg; 6–12 y of age) were included. All procedures were conducted in accordance with the European convention for animal care (86–406) and the National Institutes of Health’s Guide for the Care and Use of Laboratory Animals. Animal studies were approved by the institutional Ethical Committee (Comité d’Ethique en Expérimentation Animale Protocol 10-003).

**fMRI Data Acquisition.** Monkeys were scanned on a 3-T horizontal scanner (Siemens Tim Trio) with a single transmit-receiver surface coil built in our institution and customized to monkeys. Before each scanning session, the contrast agent monocrystalline iron oxide nanoparticle (MION, Feraheme; AMAG Pharmaceuticals; 10 mg/kg, i.v.) was injected into the monkey’s saphenous vein (53) (see *SI Materials and Methods* for details). Functional images were pre-processed following the standard steps (*SI Materials and Methods*) and normalized to the anatomical template of the monkey MNI space (54) and band-pass filtered in the frequency range of interest (0.0025–0.05 Hz).

**Anatomical Dataset and Connectivity Matrices.** Anatomical data were derived from the CoCoMac2.0 (29) database ([cocomac.g-node.org](http://cocomac.g-node.org)) of axonal tract tracing studies using the Regional Map parcellation (55). This parcellation comprises 82 cortical ROIs (41 per hemisphere; *Table S1*).

We estimated both stationary and sliding window zero-lag covariance matrices for each sedation condition  $c$  and session  $s$  (26). All subsequent

analyses were performed on these connectivity matrices (*SI Materials and Methods*). To explore whether our results could be explained by slower brain dynamics under sedation, we conducted a lagged correlation analysis (Fig. S6), shifting one of the time series by one or two time points (*SI Materials and Methods*). We also explored whether our results could be replicated using the same methods while replacing the covariance matrix with the inverse covariance matrix (Fig. S7 and *SI Materials and Methods*).

**ACKNOWLEDGMENTS.** We thank the NeuroSpin support teams for help in data acquisition and analysis; Kelly Shen for kindly sharing the Kotter and Wanke atlas and the community structure of functional data; Gleb Begzin and Rembrandt Bakker for their support with the CoCoMac2.0 website, from

which the anatomical connectivity matrix was downloaded; Antoine Grigis, Elena Allen, Ronald Phlypo, Gaël Varoquaux, Maximilien Fournier, Athena Demertzis, and Fabián Pedregosa for useful suggestions and code sharing; Morgan Dupont and Wilfried Pianezzola for help on data acquisition; Alexis Amadon, Marie-France Hang, and Neurospin technical team for assistance; and Christophe Joubert and Jean-Marie Hélies for assistance concerning animal facilities. This work was supported by Institut National de la Santé et de la Recherche Médicale, the Avenir program (B.J.), Commissariat à l'Energie Atomique, Collège de France, ERC Grant NeuroConsc (to S.D.), Foundation Bettencourt-Schuller, and the Roger de Spoelberch Foundation. M.S. is sponsored by Consejo Nacional de Investigaciones Científicas y Técnicas (Argentina) and the James McDonnell Foundation 21st Century Science Initiative in Understanding Human Cognition–Scholar Award.

1. Raichle ME, et al. (2001) A default mode of brain function. *Proc Natl Acad Sci USA* 98(2):676–682.
2. Fox MD, et al. (2005) The human brain is intrinsically organized into dynamic, anti-correlated functional networks. *Proc Natl Acad Sci USA* 102(27):9673–9678.
3. Sporns O, Zwi JD (2004) The small world of the cerebral cortex. *Neuroinformatics* 2(2):145–162.
4. Dosenbach NU, et al. (2007) Distinct brain networks for adaptive and stable task control in humans. *Proc Natl Acad Sci USA* 104(26):11073–11078.
5. Spreng RN, Mar RA, Kim AS (2009) The common neural basis of autobiographical memory, prospection, navigation, theory of mind, and the default mode: A quantitative meta-analysis. *J Cogn Neurosci* 21(3):489–510.
6. Buckner RL, Andrews-Hanna JR, Schacter DL (2008) The brain's default network: Anatomy, function, and relevance to disease. *Ann N Y Acad Sci* 1124:1–38.
7. Christoff K, Gordon AM, Smallwood J, Smith R, Schooler JW (2009) Experience sampling during fMRI reveals default network and executive system contributions to mind wandering. *Proc Natl Acad Sci USA* 106(21):8719–8724.
8. Mason MF, et al. (2007) Wandering minds: The default network and stimulus-independent thought. *Science* 315(5810):393–395.
9. Barttfeld P, et al. (2012) State-dependent changes of connectivity patterns and functional brain network topology in autism spectrum disorder. *Neuropsychologia* 50(14):3653–3662.
10. Lu H, et al. (2012) Rat brains also have a default mode network. *Proc Natl Acad Sci USA* 109(10):3979–3984.
11. Vincent JL, et al. (2007) Intrinsic functional architecture in the anaesthetized monkey brain. *Nature* 447(7140):83–86.
12. Fernández-Espejo D, et al. (2012) A role for the default mode network in the bases of disorders of consciousness. *Ann Neurol* 72(3):335–343.
13. Guldenmund P, Vanhaudenhuyse A, Boly M, Laureys S, Soddu A (2012) A default mode of brain function in altered states of consciousness. *Arch Ital Biol* 150(2–3):107–121.
14. Monti MM, et al. (2010) Willful modulation of brain activity in disorders of consciousness. *N Engl J Med* 362(7):579–589.
15. Owen AM, et al. (2006) Detecting awareness in the vegetative state. *Science* 313(5792):1402.
16. Deco G, Jirsa VK, McIntosh AR (2013) Resting brains never rest: Computational insights into potential cognitive architectures. *Trends Neurosci* 36(5):268–274.
17. Deco G, et al. (2014) Identification of optimal structural connectivity using functional connectivity and neural modeling. *J Neurosci* 34(23):7910–7916.
18. Casali AG, et al. (2013) A theoretically based index of consciousness independent of sensory processing and behavior. *Sci Transl Med* 5(198):ra105.
19. Sitt JD, et al. (2014) Large scale screening of neural signatures of consciousness in patients in a vegetative or minimally conscious state. *Brain* 137(Pt 8):2258–2270.
20. Naci L, Cusack R, Anello M, Owen AM (2014) A common neural code for similar conscious experiences in different individuals. *Proc Natl Acad Sci USA* 111(39):14277–14282.
21. Deco G, Jirsa VK, McIntosh AR (2011) Emerging concepts for the dynamical organization of resting-state activity in the brain. *Nat Rev Neurosci* 12(1):43–56.
22. Dehaene S, Changeux JP (2011) Experimental and theoretical approaches to conscious processing. *Neuron* 70(2):200–227.
23. Hudetz AG, Liu X, Pillay S (2014) Dynamic repertoire of intrinsic brain states is reduced in propofol-induced unconsciousness. *Brain Connect*, 10.1089/brain.2014.0230.
24. Oizumi M, Albantakis L, Tononi G (2014) From the phenomenology to the mechanisms of consciousness: Integrated Information Theory 3.0. *PLOS Comput Biol* 10(5):e1003588.
25. Moeller S, Nallasamy N, Tsao DY, Freiwald WA (2009) Functional connectivity of the macaque brain across stimulus and arousal states. *J Neurosci* 29(18):5897–5909.
26. Allen EA, et al. (2014) Tracking whole-brain connectivity dynamics in the resting state. *Cereb Cortex* 24(3):663–676.
27. Chang C, Glover GH (2010) Time-frequency dynamics of resting-state brain connectivity measured with fMRI. *Neuroimage* 50(1):81–98.
28. Hutchison RM, Wormsley T, Gati JS, Everling S, Menon RS (2013) Resting-state networks show dynamic functional connectivity in awake humans and anesthetized macaques. *Hum Brain Mapp* 34(9):2154–2177.
29. Bakker R, Wachtler T, Diesmann M (2012) CoCoMac 2.0 and the future of tract-tracing databases. *Front Neuroinform* 6:30.
30. Hutchison RM, et al. (2013) Dynamic functional connectivity: Promise, issues, and interpretations. *Neuroimage* 80:360–378.
31. Shen K, et al. (2012) Information processing architecture of functionally defined clusters in the macaque cortex. *J Neurosci* 32(48):17465–17476.
32. Rubinov M, Sporns O (2010) Complex network measures of brain connectivity: Uses and interpretations. *Neuroimage* 52(3):1059–1069.
33. Sporns O, Chialvo DR, Kaiser M, Hilgetag CC (2004) Organization, development and function of complex brain networks. *Trends Cogn Sci* 8(9):418–425.
34. Markov NT, et al. (2013) Cortical high-density counterstream architectures. *Science* 342(6158):1238406.
35. Tagliazucchi E, et al. (2013) Breakdown of long-range temporal dependence in default mode and attention networks during deep sleep. *Proc Natl Acad Sci USA* 110(38):15419–15424.
36. Li Y, Qiu J, Yang Z, Johns EJ, Zhang T (2008) Long-range correlation of renal sympathetic nerve activity in both conscious and anesthetized rats. *J Neurosci Methods* 172(1):131–136.
37. Dehaene S, Changeux JP (2005) Ongoing spontaneous activity controls access to consciousness: a neuronal model for inattentional blindness. *PLoS Biol* 3(5):e141.
38. Ghosh A, Rho Y, McIntosh AR, Kotter R, Jirsa VK (2008) Noise during rest enables the exploration of the brain's dynamic repertoire. *PLOS Comput Biol* 4(10):e1000196.
39. Petermann T, et al. (2009) Spontaneous cortical activity in awake monkeys composed of neuronal avalanches. *Proc Natl Acad Sci USA* 106(37):15921–15926.
40. Boveroux P, et al. (2010) Breakdown of within- and between-network resting state functional magnetic resonance imaging connectivity during propofol-induced loss of consciousness. *Anesthesiology* 113(5):1038–1053.
41. Ferrarelli F, et al. (2010) Breakdown in cortical effective connectivity during midazolam-induced loss of consciousness. *Proc Natl Acad Sci USA* 107(6):2681–2686.
42. King JR, et al. (2013) Information sharing in the brain indexes consciousness in non-communicative patients. *Curr Biol* 23(19):1914–1919.
43. Lewis LD, et al. (2012) Rapid fragmentation of neuronal networks at the onset of propofol-induced unconsciousness. *Proc Natl Acad Sci USA* 109(49):E3377–E3386.
44. Alkire MT, Hudetz AG, Tononi G (2008) Consciousness and anesthesia. *Science* 322(5903):876–880.
45. Murphy K, Birn RM, Handwerker DA, Jones TB, Bandettini PA (2009) The impact of global signal regression on resting-state correlations: are anti-correlated networks introduced? *Neuroimage* 44(3):893–905.
46. Marois R, Ivanoff J (2005) Capacity limits of information processing in the brain. *Trends Cogn Sci* 9(6):296–305.
47. Dehaene S, Charles L, King JR, Martí S (2014) Toward a computational theory of conscious processing. *Curr Opin Neurobiol* 25:76–84.
48. Schnakers C, et al. (2009) Diagnostic accuracy of the vegetative and minimally conscious state: clinical consensus versus standardized neurobehavioral assessment. *BMC Neurol* 9:35.
49. King JR, et al. (2013) Single-trial decoding of auditory novelty responses facilitates the detection of residual consciousness. *Neuroimage* 83:726–738.
50. Boly M, et al. (2008) Intrinsic brain activity in altered states of consciousness: how conscious is the default mode of brain function? *Ann N Y Acad Sci* 1129:119–129.
51. Boly M, et al. (2009) Functional connectivity in the default network during resting state is preserved in a vegetative but not in a brain dead patient. *Hum Brain Mapp* 30(8):2393–2400.
52. Vanhaudenhuyse A, et al. (2010) Default network connectivity reflects the level of consciousness in non-communicative brain-damaged patients. *Brain* 133(Pt 1):161–171.
53. Vanduffel W, et al. (2001) Visual motion processing investigated using contrast agent-enhanced fMRI in awake behaving monkeys. *Neuron* 32(4):565–577.
54. Frey S, et al. (2011) An MRI based average macaque monkey stereotaxic atlas and space (MNI monkey space). *Neuroimage* 55(4):1435–1442.
55. Kotter R, Wanke E (2005) Mapping brains without coordinates. *Philos Trans R Soc Lond B Biol Sci* 360(1456):751–766.

# Supporting Information

Barttfeld et al. 10.1073/pnas.1418031112

## SI Materials and Methods

### Propofol Anesthesia.

**Administration.** Monkeys were scanned in an awake resting condition and under two different levels of propofol sedation: moderate propofol sedation and deep propofol sedation (general anesthesia) defined by the monkey sedation scale (Table S1) and EEG. The monkeys were trained for i.v. propofol injection in the awake condition (5–7.5 mg/kg i.v.; Fresenius Kabi) in the saphenous vein for induction of sedation. Sedation was maintained using a target controlled infusion (TCI) system (Alaris PK Syringe pump; CareFusion) based on the Paedfusor pharmacokinetic model (1) for propofol. The TCI of propofol was 3.7–4.5 µg/mL for the moderate propofol sedation condition and 5.8–6.5 µg/mL for the deep propofol sedation condition. Muscle blocking agent (cisatracrium, 0.15 mg/kg bolus i.v., followed by continuous i.v. infusion at a rate of 0.18 mg/kg/h; GlaxoSmithKline) was used to avoid artifacts related to potential movements during moderate propofol sedation. Under sedation, all monkeys were intubated (Rüsch; Teleflex Medical; cuffed tube, internal diameter 4–4.5 mm) and mechanically ventilated (Aestiva/5 MRI; General Electric Healthcare) (tidal volume: 8–10 mL/kg; respiration rate of 23–31/min, end-tidal CO<sub>2</sub> of 40–42 mmHg, FiO<sub>2</sub> = 0.5). Physiological monitoring included heart rate, noninvasive blood pressure [systolic blood pressure, diastolic blood pressure, mean blood pressure, oxygen saturation (SpO<sub>2</sub>), respiratory rate, end-tidal CO<sub>2</sub> (EtCO<sub>2</sub>), cutaneous temperature]. All physiological parameters were recorded with a digital recording system (Maglife; Schiller). i.v. hydration was ensured by a mixture of normal saline (0.9%) and 5% glucose (250 mL of normal saline with 100 mL of 5% glucose) at a rate of 10 mL/kg/h. At the end of each fMRI scanning session, anesthesia was stopped, and the animal was monitored carefully during recovery. The animal was then placed in individual housing and monitored until full recovery from anesthesia.

**Monitoring of anesthesia depth.** We used both behavioral testing and EEG (see EEG methods below and Table S1) to define the anesthesia depth. The levels of arousal were defined using the Monkey Sedation scale, a clinical sedation scale that was adapted from the Human Observer's Assessment of Alertness/Sedation scale (2) and a previously described monkey arousal scale (3). At each fMRI session, the clinical score was determined at the beginning and the end of the scanning session. The clinical scale is based on spontaneous movements and the response to different stimuli (juice presentation, shaking/prodding, toe pinch) and corneal reflex (Table S1). In awake condition, monkeys scored positive in all items considered. Propofol monotonically caused negative responses to stimulation and spontaneous activity. Under moderate sedation, monkeys also stopped showing spontaneous movements while still tended to respond to shaking/prodding. Finally, under deep sedation monkeys stopped responding to all stimuli, reaching a state of general anesthesia.

**EEG acquisition and analysis.** We acquired EEG scalp recordings using a customized EEG cap (EasyCap, 13 channels), an MR amplifier (BrainAmp; Brain Products), and the Vision Recorder software (Brain Products). Parameters were as follow: sampling rate, 5,000 per channel; impedance, <20 MΩ; band-pass filtered 0.01 Hz < f < 500 Hz during collection. We applied an EEG gel to obtain low impedances (One Step EEG gel; Germany). To check the anesthesia level, EEG scalp recordings were acquired before entering the scanner room (10 min before starting MRI acquisition). We performed an online analysis through visual assessment of EEG traces. We interpreted the EEG traces vi-

sually and defined the EEG based levels of sedation for clinical sedative level (Table S1). Levels of sedation were defined as follow: level 1, awake condition, posterior alpha waves (eyes closed) and anterior beta waves; level 2, light propofol sedation, no fMRI data collection at this level, increasing of the amplitude of alpha waves and anterior diffusion of alpha waves; level 3, moderate propofol sedation, diffuse and wide alpha waves, and anterior theta waves (4); level 4, deep propofol sedation (general anesthesia), diffuse delta waves, waves of low amplitude (5, 6) and anterior alpha waves (10 Hz) (7); level 5, very deep sedation (deeper than level of general anesthesia), burst suppression (no fMRI data collection at this sedation level).

**fMRI Data Acquisition.** Monkeys were scanned on a 3-T horizontal scanner (Siemens Tim Trio) with a single transmit-receiver surface coil built in our institution and customized to monkeys. Each functional scan consisted of gradient-echoplanar whole-brain images (TR, 2,400 ms; TE, 20 ms; and 1.5-mm<sup>3</sup> voxel size; 500 brain volumes per session). For the awake condition, monkeys were implanted with an MR-compatible headpost and trained to sit in the sphinx position in a primate chair (8, 9). Monkeys sat in the dark inside the MRI without any task. The eye position was monitored at 120 Hz (Iscan Inc.). For the anesthesia sessions, animals were positioned in a sphinx position in the MR scanner and mechanically ventilated, and their physiological parameters were monitored. Seventy-seven sessions were performed, divided as follows: 21 awake sessions (monkey J: 16 sessions; monkey K: 5 sessions; monkey R: no awake session), 25 moderate propofol sedation sessions (monkey J: 2 sessions; monkey K: 11 sessions; monkey R: 12 sessions), and 31 deep propofol sedation sessions (monkey J: 9 sessions; monkey K: 10 sessions; monkey R: 12 sessions).

**fMRI Preprocessing.** Functional images were slice-time corrected, reoriented, realigned, and unwarped to correct for susceptibility-by-movement interaction, resampled (1-mm isotropic), rigidly coregistered to the anatomical template of the monkey MNI space (10), and smoothed (Gaussian kernel, 3-mm full width at half maximum) using FSL ([www.fmrib.ox.ac.uk/fsl/](http://www.fmrib.ox.ac.uk/fsl/)) and custom Python code (8). We also removed by regression the movement parameters resulting from rigid body correction for head motion (11), as well as the global signal. We regressed out global signal from the images to rule out any confounding effect due to physiological (e.g., respiratory and cardiac) changes associated to propofol administration. Voxel time series were filtered with high-pass (0.0025-Hz cutoff) and low-pass (0.05 Hz cutoff) filters and with a zero-phase fast-Fourier (FFT) notch filter (0.03 Hz) to remove an artifactual pure frequency present in all sessions. Following a previous study (12), we normalized the variance of each time series; thus, covariance matrices correspond to correlation matrices.

**Anatomical Dataset and Functional Atlas.** Anatomical data were derived from the CoCoMac2.0 (13) database ([cocomac.g-node.org](http://cocomac.g-node.org)) of axonal tract tracing studies using the Regional Map parcellation (14). This parcellation comprises 82 cortical ROIs (41 per hemisphere; Table S1). This anatomical connectivity matrix included interhemispheric connections. All connections were mirror-symmetrical across hemispheres. When information about the connectivity between two regions was not available in CoCoMac, the connection strength was set to 0 (15). The CoCoMac connectivity matrix classifies the strength of the

anatomical connections as weak, moderate or strong, codified as 1, 2, and 3, respectively. Following Shen et al. (15), when a description of strength was not provided, the connection strength was set to moderate.

The Regional Map parcellation was drawn on the F99 macaque standard cortical surface template (16, 17) and coregistered to the MNI space. Brain renders were done using custom Matlab scripts based on scripts by Gleg Begzin available at CoCoMac 2.0 webpage.

**Stationary Connectivity Analysis.** We estimated for each sedation condition  $c$  and session  $s$  the covariance matrix  $C_{c,s}$ , to confirm the presence of long-range stationary connections under awake and anesthesia (18, 19). To this aim, for each ROI, a time series was extracted for each session  $s$ , averaging all voxels within a ROI at a given brain volume. The matrix entry  $C_{c,s}(i,j)$  indicates the temporal correlation of the average fMRI signal of ROIs  $i$  and  $j$ , which henceforth is referred as stationary functional connectivity. We estimated covariance from the regularized precision matrix (20). Following the graphical LASSO method (21), we placed a penalty on the L1 norm of the precision matrix to promote sparsity [the regularization parameter lambda ( $\lambda$ ) was set to 0.1]. Through this method, we obtained a connectivity matrix per sedation condition and session, sized  $82 \times 82$ , which was Fisher transformed before further analysis as  $z = ar \tanh(c)$  to obtain the  $Z_{c,s}$  matrix.

Fig. 1A shows the average of this matrix,  $Z_c$ , one per sedation condition (Fig. 1A). To test for statistical significance of connectivity between brain regions in different sedation conditions, Student  $t$  tests were performed with the null hypothesis of zero correlation. To correct for the multiple comparisons, the false discovery rate (FDR) method was used, with a  $P$  value of 0.0001. To promote sparsity in the brain renders, we plotted into glass brains all significant connections that also displayed absolute connectivity strength higher than 0.3 (Fig. 1 B–D).

To characterize  $Z_{c,s}$  matrices, we calculated for each sedation condition  $c$  and session  $s$  the average of positive z-values of  $Z_{c,s}$  and also the rate between negative and positive z-values. We assessed significant differences between sedation conditions through a bootstrapping method (22) as follows: we obtained for every sedation condition and session the mean value of all positive connection of every ROI, as

$$Z_{c,Positive} = \sum_{i=1}^N \frac{Z_{pos,c,s}(i,j)}{N} \quad \text{if } i \neq j,$$

where  $Z_{pos}$  represents all z-values that are positive in a matrix  $Z_{c,s}$  and  $N$  is the total number of positive z-values. After calculating  $Z_{c,Positive}$ , we subtracted the mean value of two condition (for instance,  $Z_{awake,Positive} - Z_{deep,Positive}$ ), and called it the observed difference between conditions. We calculated the null distribution of  $Z_{c,Positive}$  values differences between conditions shuffling scanning sessions across conditions (thus, breaking any possible dependence between sedation condition and connectivity value) and repeated the subtraction analysis 100,000 times, obtaining a distribution of random mean z-values differences that approaches a Gaussian distribution. This distribution is called null distribution and is the distribution of expected differences under the hypothesis of no relation between sedation condition and mean positive connectivity. If our observed difference in  $Z_{c,Positive}$  is truly reflecting a difference between sedation conditions, its value should be located on a tail of the null distribution. We fitted a Gaussian to the null distribution to obtain a normalized  $Z_{c,Positive}$ , by subtracting to the observed  $Z_{c,Positive}$  the mean value of the fitted Gaussian and dividing it by the SD of the Gaussian distribution. We obtained the  $P$  value corresponding to the normalized  $Z_{c,Positive}$  as the cumulative probability

to the normalized observed difference in the normalized Gaussian distribution. This procedure was used each time a bootstrap analysis is performed in this work.

We also calculated for each condition  $c$  and each session  $s$  the rate of negative to positive z-values to quantify changes in negative z-values across conditions, as

$$\text{rate}_{c,s} = \frac{\sum_{i=1}^N \sum_{j=1}^N \text{abs}(Z_{i,j}) | Z_{i,j} < 0}{\sum_{i=1}^N \sum_{j=1}^N Z_{i,j} | Z_{i,j} > 0}.$$

#### Dynamical Connectivity Analysis.

**Dynamical connectivity matrices.** We estimated the sliding window covariance matrix  $C_{c,s,w}$ , for each sedation condition  $c$ , session  $s$ , and time window  $w = 1 \dots W$  (12). We computed covariance matrices from windowed segments of the time series. We used a Hamming window (width = 35 scans), sliding with steps of 1 scan, resulting in  $W = 464$  windows per session. Because short time segments may have insufficient information to characterize the full covariance matrix, we estimated covariance from the regularized precision matrix (20). As done for the stationary analysis, we placed a penalty on the L1 norm of the precision matrix to promote sparsity (the regularization parameter  $\lambda$  was set to 0.1). This procedure resulted, for each condition  $c$  and session  $s$ , in a 3D matrix  $C_{c,s,w}$  sized  $82 \times 82 \times 464$ , which was Fisher transformed ( $Z_{c,s,w}$ ) before further analysis.

**Unsupervised clustering and brain states.** To assess the structure of reoccurring connectivity patterns, we applied the  $k$ -means clustering algorithm (23) to  $Z_{c,s,w}$  matrices, using the L1 distance function (Manhattan distance), as implemented in Matlab (MathWorks). Covariance values between all ROIs were included, resulting in  $[82 \times (82 - 1)]/2 = 3,321$  features per matrix. Before clustering,  $Z_{c,s,w}$  matrices were subsampled along the time dimension ( $w$ ). Subsampling was performed to reduce redundancy between windows (12). The sampled connectivity matrices ( $Z_{examples,c,s}$ ) were chosen as those windows with local maxima in functional connectivity variance (those peaks where the absolute normalized variance was higher than 0.5 SDs), resulting in  $9.6 \pm 2.54$  (mean  $\pm$  SD) windows or examples per session, for a total of 6,724 instances (samples from the  $Z_{c,s,w}$  matrix). The clustering algorithm was applied to the  $Z_{examples,c,s}$  and was repeated 500 times to increase chances of escaping local minima, with random initialization of centroid positions. The resulting centroids or median clusters (called  $BS_n$  with  $n = 1 \dots 7$ ; each  $BS_n$  is sized  $82 \times 82$ ) were then used to initialize a clustering of all data, i.e., not only the examples but the entire  $Z_{c,s,w}$  matrices (77 fMRI sessions  $\times$  464 windows = 35,728 instances), obtaining a matrix of brain states  $B_{c,s,w}$ , which, for a given sedation condition  $c$  and session  $s$ , is a vector of length 464, valued 1–7 (the predefined number of clusters), because each matrix in  $Z_{s,p,w}$  is assigned a  $BS_n$ . The number of clusters  $k$  (or brain states) was determined following ref. 12, although additional exploratory analyses varying  $k$  from 5 to 10 demonstrated consistent and robust results over a large range of  $k$  (Fig. S1).

**Similarity score and probability of each state.** To investigate the dependence of brain dynamics and sedation condition, we defined a measure of similarity between anatomical connectivity as provided by CoCoMac2.0 and functional connectivity, to rank all brain states along this dimension. The similarity score was computed by measuring the correlation coefficient between the vectorized structural matrix (sized  $6,724 \times 1$ ) and each vectorized brain state or centroid from the clustering analysis (using the Euclidean distance instead of correlation or only positive values of the brain states to calculate the correlation, did not qualitatively changed the results; Fig. S3). Using the similarity score, we ranked all brain states in ascending order of similarity to structure (Fig. 2 A and B).

To calculate probability of occurrence of any brain state (Fig. 2D) we obtained, for each sedation condition  $c$  and each brain state  $n$ , the percentage of occurrence as

$$P_{c,n} = \frac{\sum_{i=1}^N (B_{c,s,i} = n)}{N},$$

in which  $n = 464$ . For each session,  $P_c$  adds up to 1. We calculated the SEM through a jackknife procedure (24), as follows: for each sedation condition  $c$ , we repeated the estimation of probability of occurrence for every brain state  $n$  ( $P_{c,n}$ ),  $N - 1$  times ( $N$  is the number of sessions within each sedation condition), each time excluding a different session from the analysis; SEM is then calculated as  $sem_{c,x} = \text{sqrt}(P_{c,n})*(N - 1)$ .

To quantify the relation between probability of occurrence and similarity score, we conducted, for each sedation condition, a regression analysis, to quantify the beta value ( $\beta$ ), the  $R^2$ , and a  $P$  value. Differences in brain state composition across vigilance conditions were assessed through a fixed-effects ANOVA, with mean rank similarity, that is, the result of averaging each brain state time series, valued from 1 (the less similar to structure brain state) to 7 (the more similar to structure brain state), as a dependent variable and the vigilance condition as the independent variable. We also run a fixed effects ANOVA to quantify the effect of sedation on the probability of brain state 7. For this, we followed the same procedure, but the mean rank similarity was calculated considering only the presence of brain state 7 (window  $w$  valued at 1) or any other state (window  $w$  valued at 0).

**Topology and network properties of brain states.** Fig. S2 shows several views of the brain states ordered according to their similarity score. Fig. S2A shows all connections, both positive and negative, above a threshold of  $z = 0.5$ . Fig. S2B shows the top 400 links of each brain state to explore the connectivity pattern dominating in each vigilance condition. We see that brain state 1 shows a clear characteristic pattern, with positive connections forming a frontoparietal core and negative connections showing long-range connections linking frontal and occipital regions. This pattern changes along the similarity axis, and brain state 7 presents a much more diffuse pattern, lacking a central core of positive connections. Fig. S2C shows the top 30 connected ROIs for each brain state. ROI size codifies the normalized number of connections. Fig. S2D shows the minimal energy plots of the brain states: using the Kamada–Kawai algorithm (25), we embedded the top 2,500 links of each brain state in the 2D plane. Resulting graphs show that networks are qualitatively different: brain states with low similarity score clearly show two sub-components of the network, a subdivision that is completely lost in brain state 7 (despite having equal number of links; Fig. 2D).

Fig. 2H shows the normalized probability distribution of  $z$ -values for brain states 1 and 7, binning correlation values in 45 bins. Fig. 2I and J shows the 2D normalized histograms of the same brain states  $z$ -values, as a function of distance between pairs of ROIs. Distance was between ROIs was calculated as the L2 norm in the 3D space, using MNI coordinates of CoCoMac as input.

Fig. 2K shows the four communities obtained from Shen et al. (15). For every brain state  $n$ , we calculated the absolute average correlation between all ROIs belonging to community  $i$  and all ROIs belonging to community  $j$ . To observe inter- and intra-community mean correlation along the similarity axis, we conducted a regression, for every pair of communities, between the absolute value of correlation and the similarity score (Fig. 2L). We observe that, after Bonferroni correction, only correlations between communities 3 and 4 and between communities 3 and 1 significantly diminished as a function of similarity to structure. We set the  $P$  value at 0.05, Bonferroni corrected for multiple comparisons (10 possible community combinations). We also

calculated for each brain state  $n$  the ratio intermodule vs. intramodule correlations, and we conducted a regression between this ratio and the similarity score (Fig. 2M).

We used a graph theory metric, Small World (SM) index, to summarize topological information (26, 27) (Fig. 2N). Each  $BS_n$  matrix defines a weighted graph where each ROI corresponds to a node and the weight of each link is determined by the  $z$ -value between each ROI pair. To calculate SM index,  $BS_n$  matrices were converted to binary undirected matrices by applying a threshold  $T$ . The arbitrary parameter  $T$  was chosen so that in all cases the resulting networks had a link density of 0.10, i.e., 10% of the total number of possible links in the networks were actually present, to ensure that only the strongest links are present but the network is not disaggregated into subcomponents (28) and to normalize networks of different brain states by size to avoid spurious effects on the metrics due to network size. On the thresholded matrices, we calculated the clustering coefficient  $C$  and the characteristic path length  $L$  using the Brain Connectivity Toolbox (27). Combining the metrics  $C$  and  $L$ , we calculated the SM index, as  $SM = C/L$  (29). To quantify changes in SM across brain states, we conducted a regression analysis between the SM index and the similarity score.

We also quantified the duration of each brain state (that is, the average length of sequences of a given brain state in the  $B_{c,s,w}$  matrix; Fig. 2O). For each sedation condition  $c$  and session  $s$ , we computed the length of sequences composed by only one brain state. To account for the random length duration, occurring solely due to a brain state's proportion (i.e., the more likely a brain state is, the longer its sequence is expected to be), we calculated a random distribution of sequence lengths by shuffling the  $B_{c,s,w}$  5,000 times along the time dimension. We then subtracted from the observed lengths the average time expected by frequency of each brain state. We quantified differences between sedation states through a bootstrap procedure, as done before.

To investigate putative changes in long-range temporal correlation (LRTC) and its relation with brain states, we estimated, for every session  $s$ , the Hurst exponent ( $H$ ) through detrended fluctuation analysis (DFA) (30). DFA is a scaling analysis method that can be used in nonstationary time sequences. For each time series  $x$  of every session  $s$ , we subtracted its temporal mean and calculated its cumulative sum as

$$X_t = \sum_{i=1}^t (x_i - \langle x \rangle),$$

where  $\langle x \rangle$  stands for the temporal mean of the signal. The cumulative signal  $X_t$  is divided into nonoverlapping windows of length 10 samples. A linear trend is fitted to this windowed time series using least squares, and then the signal is detrended by subtracting the best linear fit, producing signal  $Y_n$ . The root-mean-square deviation (that is, the fluctuation of the signal) is calculated from the detrended windowed time series, as

$$F_L = \sqrt{1/L \sum_{k=1}^L (Y_k - Y_n)^2}.$$

Finally, the Hurst exponent is obtained by plotting in a log-log graph  $F_L$  against  $L$ . Through least squares, we obtained the slope  $\alpha$  of the relation between  $F_L$  and  $L$ . Because  $\alpha$  changes for large values of  $F_L$  and  $L$ , we estimated  $\alpha$  using the first 15 time windows ( $\alpha_1$ ). We identified the Hurst exponent with  $\alpha$ .

Fig. S5A shows  $H$  values for each ROI within the Kotter and Wanke ROI set. Renders were done using custom scripts mentioned above. Fig. S5B shows  $H$  values for each session (averaged across brain regions). To construct Fig. S5C, we calculated for

each of the 77 functional sessions its average similarity score index that is the average value of the similarity score of all  $BS_n$  with  $n = 1-7$ , within a given session. Fig. S5C plots the  $H$  value for all 77 sessions as a function of the average similarity score (color codifies vigilance condition of each session). To construct Fig. S5D, we binned average similarity score into quintiles, averaging  $H$  values within each quintile. Error bar represents 1 SE, calculated using  $n =$  number of average brain values within each quintile.

To explore the possibility that the changes observed under sedation could be due to a slower brain dynamics, we conducted a lagged correlation analysis. For this, we repeated our analyses while introducing a time lag in the calculation of covariance between ROIs  $i$  and  $j$ . For this, we shifted one of the time series by either one or two samples relative to the other. In this way we obtained a lagged correlation value between ROIs  $i$  and  $j$ . We removed from the analysis the lagged correlation of a ROI with itself, yielding a value different from 1 when introducing a time lag. Fig. S6 shows these results. Fig. S6 A and B shows time-averaged connectivity matrices for all conditions, for lag = 0 (a), lag = 1 (c), and lag = 2 (e). To build those matrices, we averaged all temporal windows from the dynamical analysis. For lag 0 we obtained extremely similar results than using the graphical Lasso covariance calculation (Fig. S6 A and B; lag 0: awake:  $\beta$ -value = 0.36;  $R^2$  = 0.13;  $P$  = 0.42; moderate:  $\beta$ -value = 0.53;  $R^2$  = 0.91;  $P$  = 0.0008; deep:  $\beta$ -value = 0.422;  $R^2$  = 0.82;  $P$  = 0.005). We found that introducing lags in the analysis did not affect our results, nor did it for lag 1 (Fig. S6 C and D; awake:  $\beta$ -value = 0.43;  $R^2$  = 0.20;  $P$  = 0.30; moderate:  $\beta$ -value = 0.54;  $R^2$  = 0.92;  $P$  = 0.0005; deep:  $\beta$ -value = 0.30;  $R^2$  = 0.85;  $P$  = 0.0031) or for lag 2 (Fig. S6

$E$  and  $F$ ; awake:  $\beta$ -value = 0.51;  $R^2$  = 0.39;  $P$  = 0.12; moderate:  $\beta$ -value = 0.47;  $R^2$  = 0.87;  $P$  = 0.0018; deep:  $\beta$ -value = 0.40;  $R^2$  = 0.84;  $P$  = 0.0037). Furthermore, the dynamical repertoire seemed to be even more depleted under sedation at larger lags, as brain state 7, the most dominant under sedation and closest to structural connectivity, became even more prominent during deep sedation as the lag increased from 0 to 2 (Fig. S6G).

To explore the robustness of our results, we also repeated the analysis using the inverse covariance matrix instead of the covariance matrix [as proposed by Allen et al. (12)]. We repeated our analysis using exactly the same methods and parameters than for covariance, mentioned above. It is known that sparsity-inducing norms such as the one used by the graphical Lasso model are not invariant under transformations such as translations and rotations (31). This invariance implies that distance similarities among covariance matrices are not necessarily translated into distance similarities among inverse covariance matrices. Nevertheless, we found that, although the results were noisier and less clear when using inverse covariance, they did not qualitatively change. We were able to reproduce the main findings: (i) modulation of brain state probability by similarity score (this time only in the deep sedation condition); (ii) strong reduction of negative links (i.e., restricting the analysis to covariance links whose inverse covariance value is different from zero) under sedation; and (iii) a shift of brain state probability as a function of sedation: in the awake condition, dominant states distant from structural connectivity are frequent, whereas under deep sedation, the brain states closest to anatomical structure dominate (Fig. S7B;  $\beta$ -value = 0.12;  $R^2$  = 0.74;  $P$  = 0.01).

1. Absalom A, Kenny G (2005) 'Paedfusor' pharmacokinetic data set. *Br J Anaesth* 95(1):110.
2. Chernik DA, et al. (1990) Validity and reliability of the Observer's Assessment of Alertness/Sedation Scale: Study with intravenous midazolam. *J Clin Psychopharmacol* 10(4):244–251.
3. Vincent JL, et al. (2007) Intrinsic functional architecture in the anaesthetized monkey brain. *Nature* 447(7140):83–86.
4. Feshchenko VA, Veselis RA, Reinsel RA (2004) Propofol-induced alpha rhythm. *Neuroscience* 50(3):257–266.
5. Murphy M, et al. (2011) Propofol anesthesia and sleep: A high-density EEG study. *Sleep* 34(3):283–91A.
6. Steriade M, Nuñez A, Amzica F (1993) A novel slow (< 1 Hz) oscillation of neocortical neurons in vivo: depolarizing and hyperpolarizing components. *J Neurosci* 13(8): 3252–3265.
7. Purdon PL, et al. (2013) Electroencephalogram signatures of loss and recovery of consciousness from propofol. *Proc Natl Acad Sci USA* 110(12):E1142–E1151.
8. Uhrig L, Dehaene S, Jarraya B (2014) A hierarchy of responses to auditory regularities in the macaque brain. *J Neurosci* 34(4):1127–1132.
9. Vanduffel W, et al. (2001) Visual motion processing investigated using contrast agent-enhanced fMRI in awake behaving monkeys. *Neuron* 32(4):565–577.
10. Frey S, et al. (2011) An MRI based average macaque monkey stereotaxic atlas and space (MNI monkey space). *Neuroimage* 55(4):1435–1442.
11. Fox MD, et al. (2005) The human brain is intrinsically organized into dynamic, anti-correlated functional networks. *Proc Natl Acad Sci USA* 102(27):9673–9678.
12. Allen EA, et al. (2014) Tracking whole-brain connectivity dynamics in the resting state. *Cereb Cortex* 24(3):663–676.
13. Bakker R, Wachtler T, Diesmann M (2012) CoCoMac 2.0 and the future of tract-tracing databases. *Front Neuroinform* 6:30.
14. Kötter R, Wanke E (2005) Mapping brains without coordinates. *Philos Trans R Soc Lond B Biol Sci* 360(1456):751–766.
15. Shen K, et al. (2012) Information processing architecture of functionally defined clusters in the macaque cortex. *J Neurosci* 32(48):17465–17476.
16. Bezgin G, Wanke E, Krummack A, Kötter R (2008) Deducing logical relationships between spatially registered cortical parcellations under conditions of uncertainty. *Neural Netw* 21(8):1132–1145.
17. Van Essen DC, et al. (2001) An integrated software suite for surface-based analyses of cerebral cortex. *J Am Med Inform Assoc* 8(5):443–459.
18. Scholvinck ML, Maier A, Ye FQ, Duyn JH, Leopold DA (2010) Neural basis of global resting-state fMRI activity. *Proc Natl Acad Sci USA* 107(22):10238–10243.
19. Logothetis NK, et al. (2012) Hippocampal-cortical interaction during periods of subcortical silence. *Nature* 491(7425):547–553.
20. Varoquaux G, Gramfort A, Poline JB, Thirion B (2010) Brain covariance selection: Better individual functional connectivity models using population prior. *Advances in Neural Information Processing Systems*, eds Zemel R, Shawe-Taylor J, Curran Associates, Inc. (Vancouver), 2334–2342.
21. Friedman J, Hastie T, Tibshirani R (2008) Sparse inverse covariance estimation with the graphical lasso. *Bioinformatics* 9(3):432–441.
22. Efron B, Tibshirani RJ (1994) *An Introduction to the Bootstrap* (Chapman and Hall, New York).
23. Lloyd S (1982) Least squares quantization in PCM. *IEEE Trans Inf Theory* 28(2):129–137.
24. Miller RG (1974) The jackknife—A review. *Biometrika* 61(1):1–15.
25. Kamada T, Kawai S (1989) An algorithm for drawing general undirected graphs. *Inf Process Lett* 31(1):7–15.
26. Sporns O, Zwi JD (2004) The small world of the cerebral cortex. *Neuroinformatics* 2(2): 145–162.
27. Rubinov M, Sporns O (2010) Complex network measures of brain connectivity: Uses and interpretations. *Neuroimage* 52(3):1059–1069.
28. Tagliazucchi E, von Wegner F, Morzelewski A, Brodbeck V, Laufs H (2012) Dynamic BOLD functional connectivity in humans and its electrophysiological correlates. *Front Hum Neurosci* 6(339):339.
29. Watts DJ, Strogatz SH (1998) Collective dynamics of 'small-world' networks. *Nature* 393(6684):440–442.
30. Peng CK, et al. (1992) Long-range correlations in nucleotide sequences. *Nature* 356(6365):168–170.
31. Yang J, Yu K, Huang T (2010) Supervised translation-invariant sparse coding. *IEEE Conference on Computer Vision and Pattern Recognition* (IEEE, San Francisco), pp 1–8.

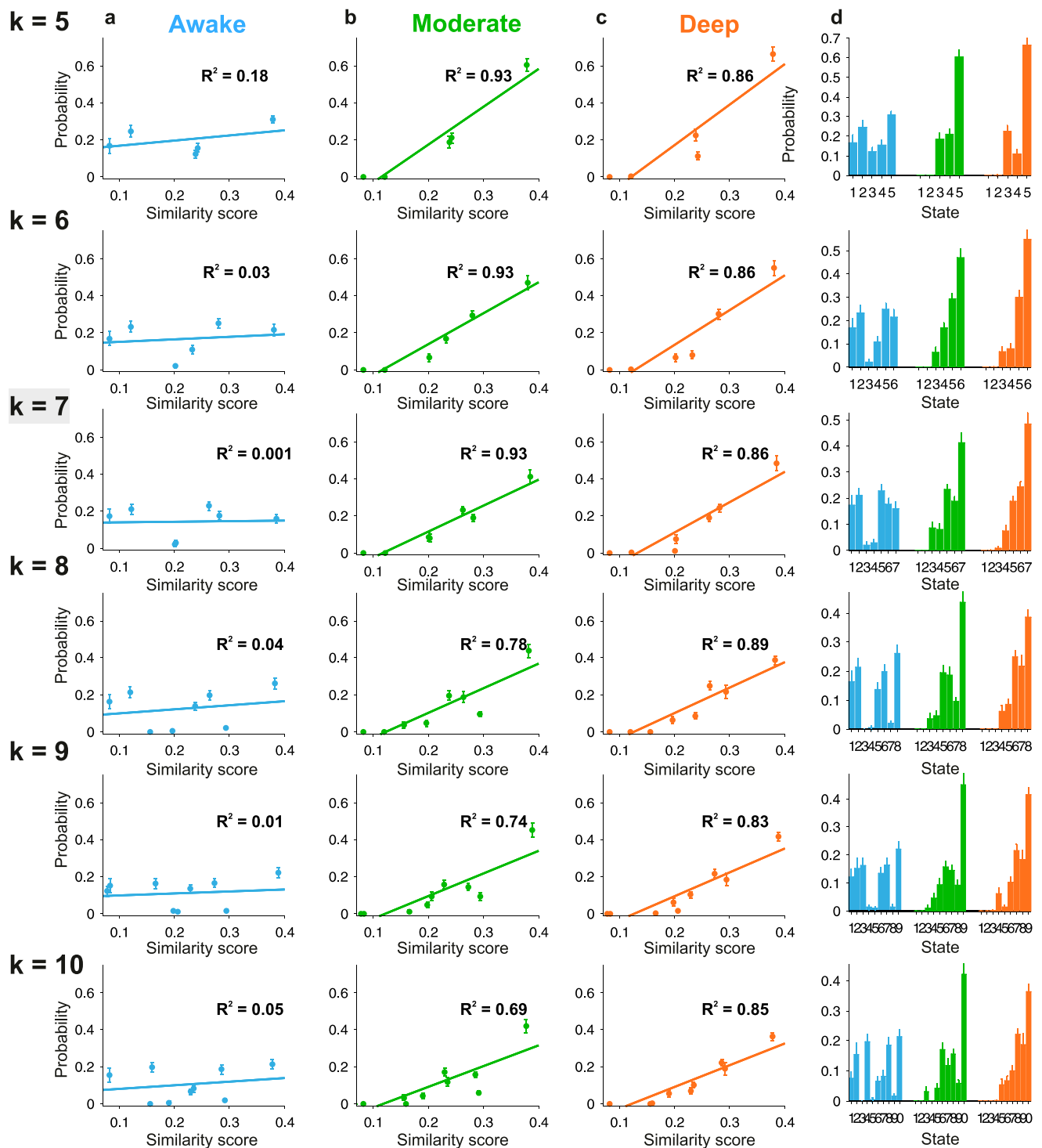


**Fig. S1.** Robustness of results with respect to the choice of a predefined number of brain states. To explore the dependence of results on the parameter  $k$  (number of predefined brain states), we explored a broad range of values for  $k = [5, 6, 7, 8, 9, 10]$  (main text only shows results for  $k = 7$ , highlighted in this figure). The relation between the probability of occurrence of a brain state and its similarity to the structural connectivity matrix for all sedation conditions (columns A–C) and the probability distributions (column D) do not significantly change with  $k$ .

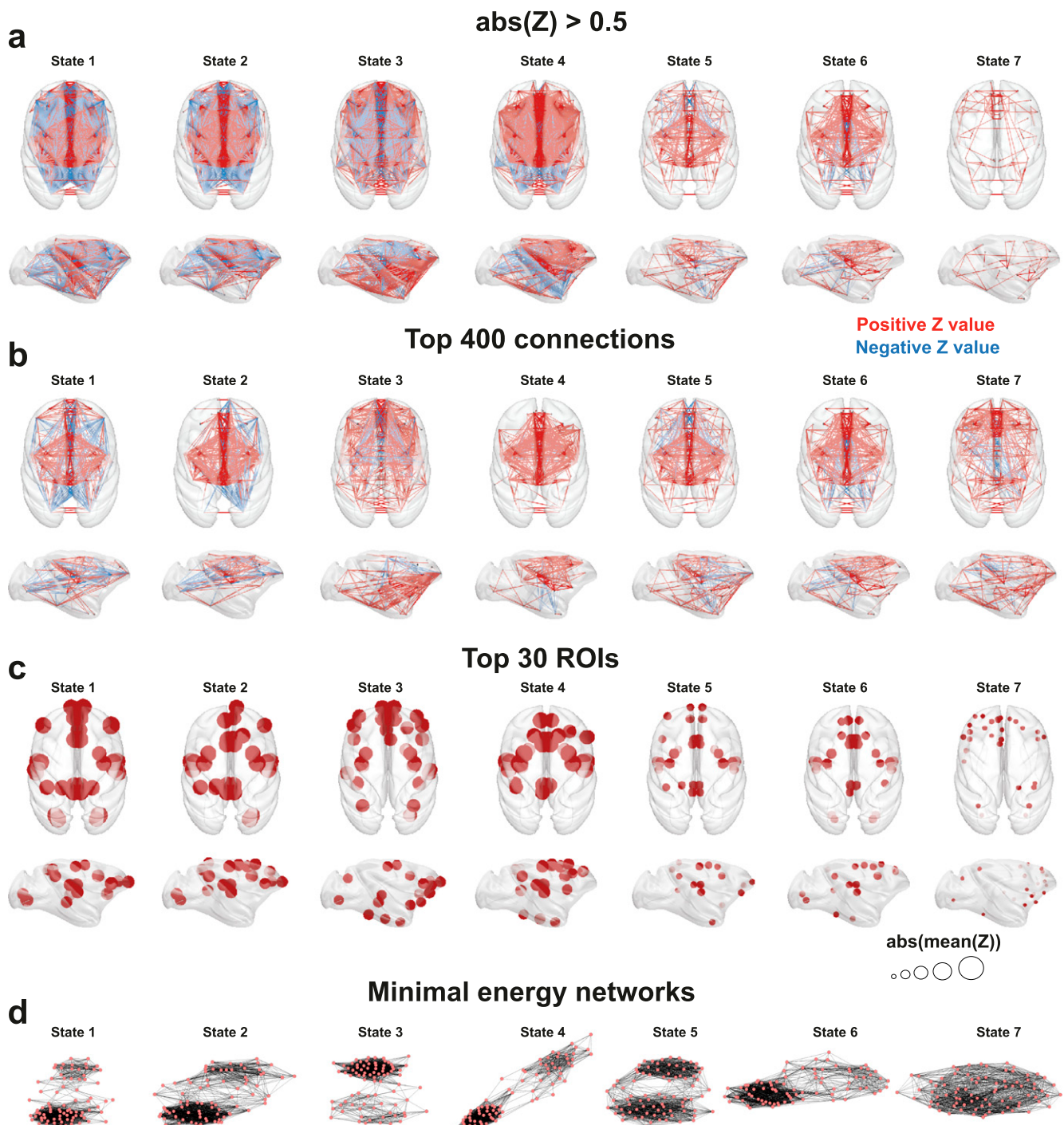


**Fig. S2.** Brain renders for the seven brain states, showing (A) the strongest connections (absolute z-value  $> 0.05$ ), (B) the strongest 400 connections, (C) the top 30 more connected ROIs, and (D) the minimal energy plots embedded in two dimensions, displaying their strongest 2,500 links embedded in the plane.

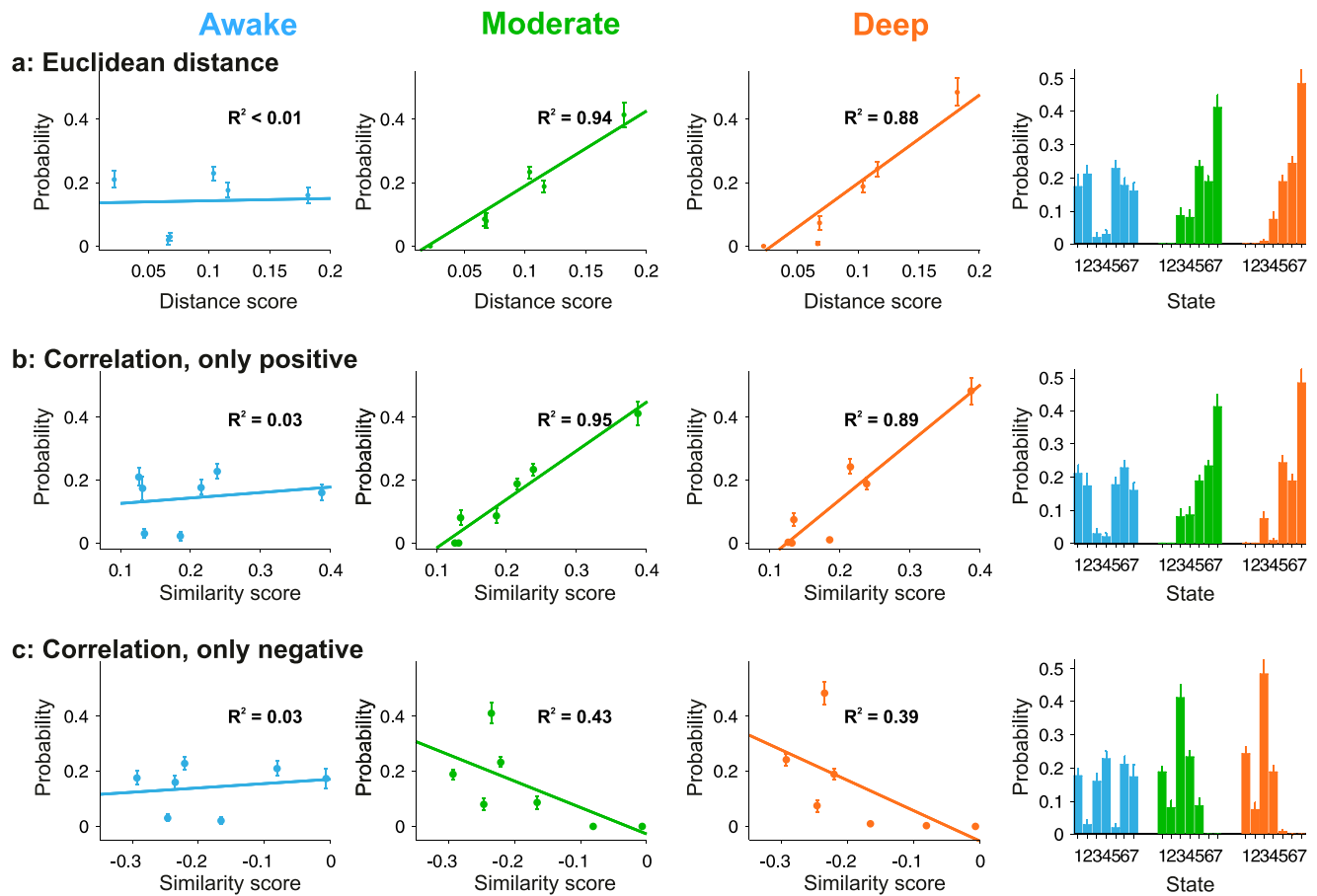


**Fig. S3.** Robustness of results with respect to alternative methods for evaluating the similarity between functional and anatomical networks. (A) Relation between probability of occurrence and similarity (Left) and probability distributions (Right) for a similarity score based on the Euclidean distance between brain state matrices and structural matrix. Probability of occurrence is plotted against the distance to anatomy (defined as  $1 - \text{similarity}$ ) to maintain the ascending slope on the curves for comparison. (B) Relation between probability of occurrence and similarity (Left) and probability distributions (Right) for a similarity calculated including only positive functional connectivity values (all negative values set to zero). (C) Same as above but including only negative correlations to calculate similarity (all positive correlations set to zero).

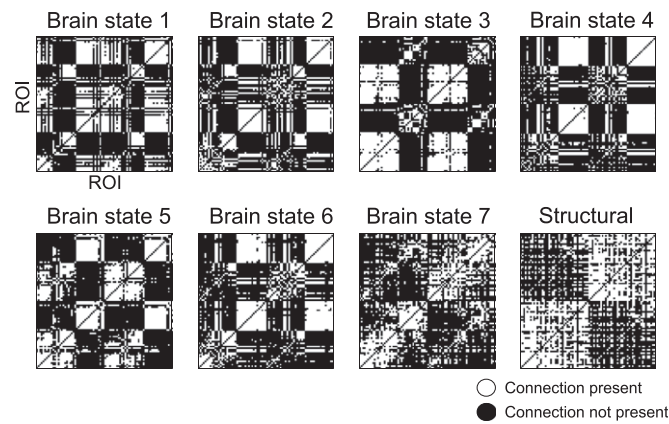


**Fig. S4.** Binarized correlation matrices showing only positive connections between ROIs for the anatomical matrix and the seven brain states. Brain states 1–6 display connectivity patterns that closely resemble the structure found in awake stationary analysis. In brain state 7, all structure is lost and positive connections spread all over the matrix, visually resembling the anatomical matrix.

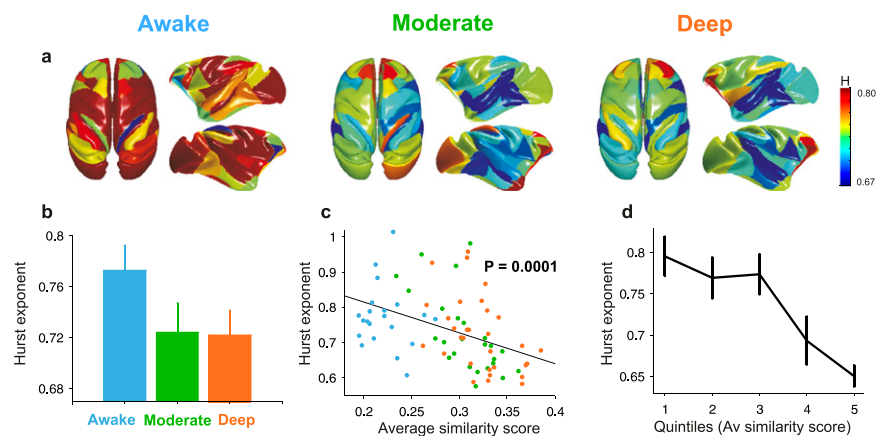


**Fig. S5.** Hurst exponent and its relation to brain states. (A) Hurst exponent value ( $H$ ) for all sessions and ROIs. (B)  $H$  value for all three conditions, averaged across regions within each session. Error bars stand for SEM. (C)  $H$  value per session (for a total of 77 sessions) as a function of the mean similarity score. (D)  $H$  values grouped into quintiles of mean similarity score.

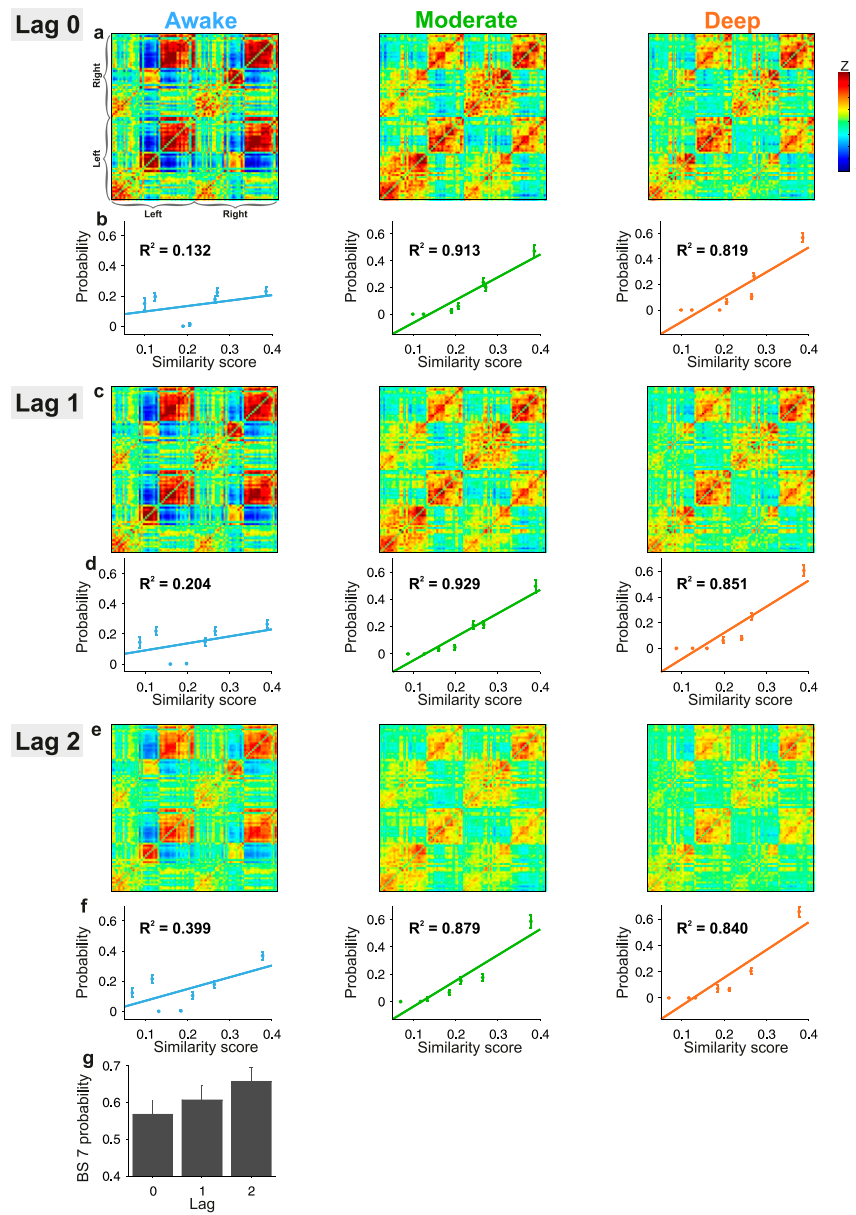


**Fig. S6.** Lagged-correlation analysis. (A, C, and E) Average connectivity matrices for all vigilance conditions, calculated by shifting the time series by zero (A), one (C), or two (E) fMRI samples (i.e., 0, 2.4, or 4.8 s). (B, D, and F) Probability of occurrence of each brain state as a function of the similarity between functional and structural connectivity for lag 0 (B), one (D), and two (F) conditions. (G) Probability of brain state 7, the dominant brain state under sedation, in deep anesthesia for lag = 0, 1, 2.

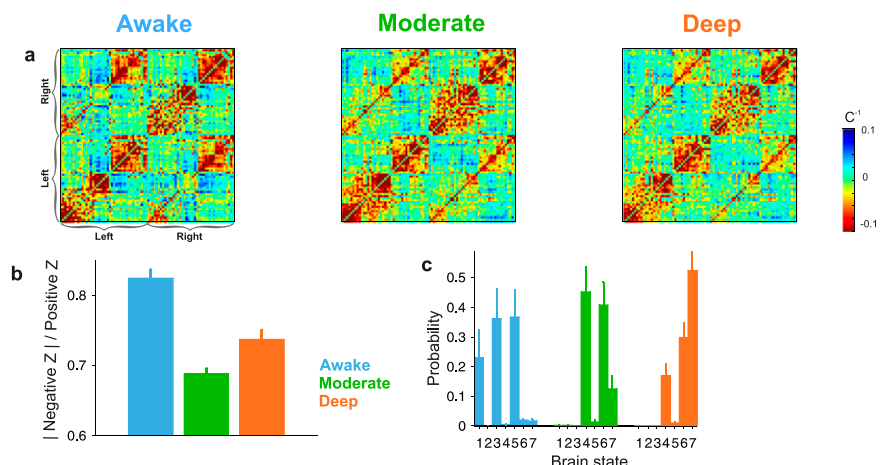


**Fig. S7.** Inverse covariance matrix and brain states. (A) Average inverse connectivity matrices for all vigilance conditions. Note that the color code is inverted for comparison with covariance matrices. (B) Rate between negative and positive covariance values considering only those connections that are different from zero in the corresponding inverse correlation matrix. (C) Probability distributions of brain states in the different vigilance conditions. Each bar represents the within-condition probability of occurrence of a state. Error bars stand for 1 SE.

**Table S1. Monkey sedation scale**

Scale	Arousal level	Juice presentation	Spontaneous movements	Shaking/prodding	Toe pinch	Corneal reflex
1	Awake	+	+	+	+	+
2	Moderate sedation	-	-	+/-	+	+
3	Deep sedation/general anesthesia	-	-	-	-	-

Juice presentation +, monkey reacts to juice presentation; spontaneous movements +, monkey moves spontaneously; shaking/prodding +, monkey has body movement, eye blinking, eye opening, or cardiac rate change during shaking/prodding; toe pinch +, monkey has body movement, eye blinking, eye opening, or cardiac rate change during toe pinching; corneal reflex +, monkey blinks eyes when cornea is stimulated.

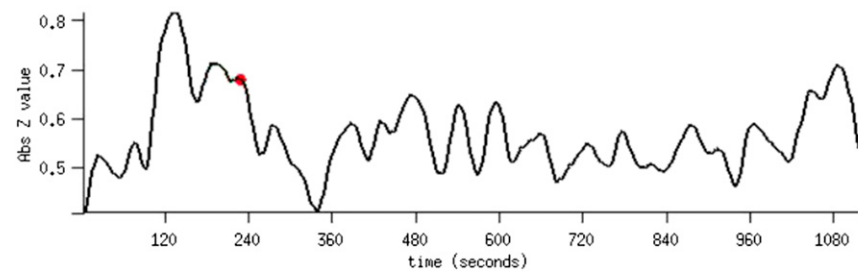
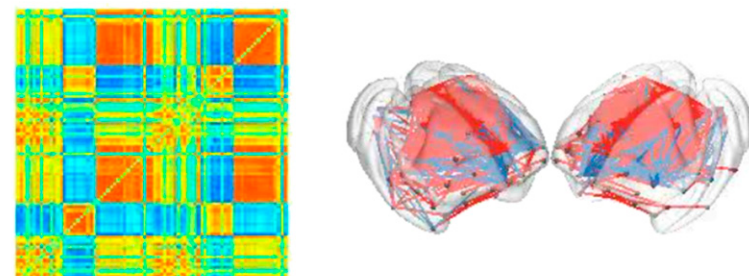
**Table S2. Functional brain atlas and community structure**

Awake	Anterior cingulate, right Primary auditory, left Secondary somatosensory, right Primary auditory, right Anterior cingulate, left Secondary somatosensory, left Secondary auditory, right Posterior cingulate, left Posterior cingulate, right Primary somatosensory, right Ventrolateral prefrontal, right Secondary auditory, left Visual area 1, right Primary somatosensory, left Primary motor, right
Moderate sedation	Primary motor, left Primary motor, right Primary somatosensory, left Primary somatosensory, right Primary auditory, left Primary auditory, right Medial premotor, right Secondary somatosensory, left Anterior cingulate, right Medial premotor, left Anterior cingulate, left Secondary somatosensory, right Dorsomedial prefrontal, left Posterior cingulate, left Secondary auditory, right Medial premotor, left Anterior cingulate, left Primary auditory, left Anterior cingulate, right Secondary sensorimotor, left Medial premotor, right Primary sensorimotor, left Primary motor, left Secondary somatosensory, right Primary auditory, right Secondary auditory, right Dorsomedial prefrontal, left Posterior cingulate, left Secondary auditory, left Primary motor, right
Deep sedation	

Labels corresponding to the 82 ROIs of the Kotter and Wanke brain atlas and their module membership. Labels correspond to the ROIs in the left hemisphere; right hemisphere is equally ordered and has an almost equivalent module membership.

**Table S3.** Top 15 ROIs with the highest average absolute value covariance in the stationary analysis

ROI label	Module
Tempolar polar	1
Superior temporal	2
Amygdala	1
Orbito Inferior prefrontal	2
Anterior insula	2
Orbitomedial prefrontal	1
Central temporal	4
Orbitomedial prefrontal	1
Inferior temporal	4
Parahippocampal	4
Gustatory	2
Ventrolateral prefrontal	2
Anterior visual area	4
Posterior insula	2
Polar prefrontal	1
Hippocampus	4
Subgenual cingulate	1
Ventrolateral prefrontal	2
Visual area 2	4
Medial prefrontal	1
Ventral temporal	4
Dorsal anterior visual area	3
Visual area 1	4
Centrolateral prefrontal	1
Secondary auditory	2
Retrosplenial cingulate	4
Posterior cingulate	2
Anterior cingulate	1
Secondary somatosensory	2
Primary somatosensory	3
Primary auditory	2
Primary motor	3
Inferior parietal	3
Medial parietal	3
Dorsomedial prefrontal	1
Intraparietal	3
Superior parietal	3
Frontal eye field	3
Dorsolateral prefrontal	1
Medial premotor	3
Dorsolateral premotor	3



**Movie S1.** Dynamical connectivity matrix for the example fMRI session shown in Fig. 1G. Brain render shows the strongest connections (absolute z value higher than 1); red lines mark positive correlations, and blue lines mark negative correlations.

[Movie S1](#)